atoms

MDPI

Article

$BAl_4Mg^{-/0/+}$: Global Minima with a Planar Tetracoordinate or Hypercoordinate Boron Atom

Maya Khatun[1], Saikat Roy [1], Sandip Giri [1], Sasanka Sankhar Reddy CH [2], Anakuthil Anoop [1,*] and Venkatesan S. Thimmakondu[3,*]

[1] Department of Chemistry, Indian Institute of Technology Kharagpur, Kharagpur 721 302, West Bengal, India; mayakhatun@iitkgp.ac.in (M.K.); saikat@iitkgp.ac.in (S.R.); sg.chem4@kgpian.iitkgp.ac.in (S.G.)
[2] Department of Electrical and Electronics Engineering, Birla Institute of Technology and Science, Pilani—K K Birla Goa Campus, Sancoale 403 726, Goa, India; sankharreddy@outlook.com
[3] Department of Chemistry and Biochemistry, San Diego State University, San Diego, CA 92182-1030, USA
* Correspondence: anoop@chem.iitkgp.ac.in (A.A.); vthimmakondusamy@sdsu.edu (V.S.T.)

Abstract: We have explored the chemical space of $BAl_4Mg^{-/0/+}$ for the first time and theoretically characterized several isomers with interesting bonding patterns. We have used chemical intuition and a cluster building method based on the tabu-search algorithm implemented in the Python program for aggregation and reaction (PyAR) to obtain the maximum number of possible stationary points. The global minimum geometries for the anion (**1a**) and cation (**1c**) contain a planar tetracoordinate boron (ptB) atom, whereas the global minimum geometry for the neutral (**1n**) exhibits a planar pentacoordinate boron (ppB) atom. The low-lying isomers of the anion (**2a**) and cation (**3c**) also contain a ppB atom. The low-lying isomer of the neutral (**2n**) exhibits a ptB atom. *Ab initio* molecular dynamics simulations carried out at 298 K for 2000 fs suggest that all isomers are kinetically stable, except the cation **3c**. Simulations carried out at low temperatures (100 and 200 K) for 2000 fs predict that even **3c** is kinetically stable, which contains a ppB atom. Various bonding analyses (NBO, AdNDP, AIM, etc.) are carried out for these six different geometries of $BAl_4Mg^{-/0/+}$ to understand the bonding patterns. Based on these results, we conclude that ptB/ppB scenarios are prevalent in these systems. Compared to the carbon counter-part, CAl_4Mg^-, here the anion (BAl_4Mg^-) obeys the 18 valence electron rule, as B has one electron fewer than C. However, the neutral and cation species break the rule with 17 and 16 valence electrons, respectively. The electron affinity (EA) of BAl_4Mg is slightly higher (2.15 eV) than the electron affinity of CAl_4Mg (2.05 eV). Based on the EA value, it is believed that these molecules can be identified in the gas phase. All the ptB/ppB isomers exhibit π/σ double aromaticity. Energy decomposition analysis predicts that the interaction between $BAl_4^{-/0/+}$ and Mg is ionic in all these six systems.

Keywords: $BAl_4Mg^{-/0/+}$; planar pentacoordinate boron; planar tetracoordinate boron; π/σ double aromaticity; global minima; chemical bonding.

Citation: Khatun, M.; Roy, S.; Giri, S.; CH, S.S.R.; Anoop, A.; Thimmakondu, V.S. $BAl_4Mg^{-/0/+}$: Global Minima with a Planar Tetracoordinate or Hypercoordinate Boron Atom. *Atoms* **2021**, *9*, 89. https://doi.org/10.3390/atoms9040089

Academic Editor:Alexander Alijah

Received: 29 September 2021
Accepted: 22 October 2021
Published: 27 October 2021

1. Introduction

From the time that the concept of planar tetracoordinate carbon (ptC) emerged [1,2], it was extended not only to its group elements (Si, Ge, Sn, etc.) [3–10] but also to other elements such as B [11–17], Al [18,19], N [20–22], P [23], O [24], and lately even to the F atom [25]. There are two main reasons why experimentalists [5,6,26–33] and theoreticians [2,34–43] have put a great deal of effort into studying these special class of molecules: (i) ptC is a fundamental deviation from the conventional ideas of tetrahedral tetracoordinate carbon [44,45]; (ii) no two structural isomers behave in the same way chemically. Thus, making this new class of molecules enhances our existing understanding about chemical bonding, and one could potentially make new materials. Schleyer and co-workers computationally identified the real local minima in lithium-substituted cyclopropane and cyclopropene molecules for the first time in 1976 [34]. In the last five decades, a large array

of molecules containing ptC atoms that are global and local minima were computationally identified [10,14,15,46–58], and some were experimentally detected [5,26–33,59]. Lately, the idea of ptC has been extended to planar hypercoordinate carbon (phC; Penta [60–66] and Hexa [67–71] coordination) and also to other elements such as B [72–75] or N [76] considering their potential applications in material science [77,78].

The idea of planar tetracoordinate boron (ptB) arrived as a byproduct of stabilizing the ptC itself. Hoffmann and co-workers, in their seminal paper [2], outlined that essentially two things are required for the electronic stabilization of the ptC atom: (1) appropriate substituents that would act as a σ-donor/π-acceptor simultaneously—that is, σ-donors would facile an electron transfer to the electron-deficient ptC atom and π-acceptors would delocalize the p_z or π-type lone pair; and (2) embedding the ptC atom into a $(4n + 2)\pi$ electron system. Considering the σ-donating and π-accepting nature of boron atoms, molecules with ptC atoms were built in the past, where boron was used as a ligating atom to the ptC atom [79,80]. Moreover, phC, phSi, and phGe molecules were also proposed computationally using boron as ligands [67,81,82]. In the strange case of CB_4, the most stable form contains a ptB atom with a tricoordinate carbon and the ptC isomer lies 1 kcal mol^{-1} above the ptB isomer, calculated using coupled-cluster methods. By altering the charge (CB_4^+), the original objective of stabilizing the ptC atom was achieved. Notably, the ptC isomer in CB_4^+ was detected through the mass spectrometry of boron carbide by Becker and Dietze [59].

Based on our earlier theoretical work on $CAl_4Mg^{-/0}$ [56], we were curious to see how replacing C with B would affect the planar tetracoordination around four Al and one Mg atoms. Thus, in this work, we analyzed the various structural isomers of $BAl_4Mg^{-/0/+}$ computationally using density functional theory (DFT). For the accurate evaluation of relative energies, composite method CBS-QB3 was used for the low-lying isomers. To our surprise, the global minimum geometries of the anion (**1a**) and cation (**1c**) contained a ptB atom (see Figure 1), whereas the global minimum of the neutral (**1n**) contained a planar pentacoordinate boron (ppB) atom. The bonding and kinetic stabilities of these three isomers along with three other key low-lying isomers **2a**; ppB, **2n**; ptB, and **3c**; ppB were studied in detail.

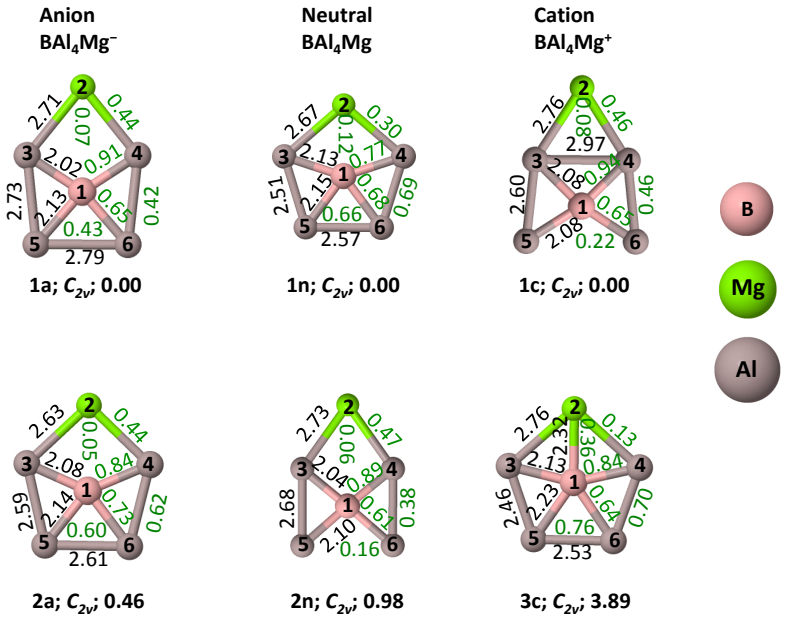

Figure 1. Global minima and low-lying isomers of $BAl_4Mg^{-/0/+}$ containing either ptB or ppB atoms. Bond lengths are given in Å and Wiberg bond indices (green color) calculated at the (U)ωB97XD/6-311++G(2d,2p) level are also shown. All isomers are minima, and ZPVE-corrected relative energies are given in kcal mol^{-1}.

2. Computational Details

Several trial geometries of $BAl_4Mg^{-/0/+}$ are generated by chemical intuition and the cluster building procedure implemented in the Python program for aggregation and reaction (PyAR) [83,84]. Modeling by intuition was conducted, targeting for ptB and ppB based on similar reported molecules. The automated cluster building was done as follows: first, a diatomic molecule was generated from two randomly chosen atoms from B, Al, and Mg. To achieve the optimized geometry of these diatomic molecules, another randomly chosen atom was added following the procedure described in [84] to generate several (N) estimated geometries. All these geometries were optimized, unique minima were chosen, and the further addition of random atoms was continued until the target chemical formula was reached. We performed 10 different runs with N = 16 orientations for the $BAl_4Mg^{-/0/+}$ systems. The trial geometries were optimized using the ORCA program [85] interfaced with PyAR [83,84]. The initial geometry optimizations were carried out using PBE [86] functional with the def2-SVP [87] basis set including Grimme's empirical dispersion corrections (D3) [88] with Becke–Johnson (BJ) damping [89,90] and resolution of identity (RI) approximation. After we filtered all geometries generated from 10 different runs, unique geometries were selected for further analysis. Some geometries were reached from both intuitive and stochastic procedures. Overall, for $BAl_4Mg^{-/0/+}$, we identified 33 stationary points, each on their singlet, doublet, and singlet potential energy surfaces, respectively.

The geometries of all $BAl_4Mg^{-/0/+}$ isomers reported here are optimized further using DFT with the (U)ωB97XD hybrid functional [91] and the 6-311++G(2d,2p) basis set [92,93]. Harmonic vibrational frequencies are calculated for each stationary point to confirm whether it is a minimum, transition state, or higher-order saddle-point. The number of imaginary frequencies (NImag) obtained for each stationary point is indicated underneath the geometries (see Figures 2–4). To obtain accurate relative energies, calculations are also conducted using the composite method, CBS-QB3 [94], for the first nine low-lying isomers (eight for cations) that lie below 20 kcal mol^{-1}. All molecules were found to have no instabilities from the wavefunction stability analysis [95] at the (U)ωB97XD/6-311++G(2d,2p) level. Triplet and quartet geometry optimization and frequency calculations were also conducted for the low-lying isomers. For brevity, triplet and quartet geometries are given in the supporting information. We carried out ab initio molecular dynamics (AIMD) simulations using the atom-centered density matrix propagation (ADMP) [96] method. These simulations were performed to check the kinetic stability of six different $BAl_4Mg^{-/0/+}$ isomers that contain ptB (**1a**, **2n**, and **1c**) or ppB atoms (**2a**, **1n**, and **3c**).

Chemical bonds in the global minima were analyzed using canonical molecular orbitals (CMOs), adaptive natural density partitioning (AdNDP) [97,98], and natural bond order (NBO) approaches [99]. Natural atomic charges (q) and Wiberg bond indices (WBIs) [100] from the NBO analyses were calculated at the (U)ωB97XD/6-311++G(2d,2p) level. Nucleus-independent chemical shift (NICS) [101] values were calculated to gauge the π/σ dual aromaticity in both global and local minima. All the above calculations were carried out with the Gaussian suite of programs [102]. An energy decomposition analysis (EDA) was performed using the Q-Chem program [103] to check the interaction between two fragments. A topological analysis of the electron localization function (ELF) and Laplacian of electron density was carried out for both the neutral and anionic global minima with the Multiwfn program [104] using the wave function file generated by the Gaussian program [102]. For brevity, optimized geometries of high-energy isomers, Cartesian coordinates of all isomers, total energies, zero-point vibrational energies (ZPVEs), net dipole moment, relative energies without and with ZPVE correction for all isomers, and kinetic stability plots of a few isomers are given in the supporting information.

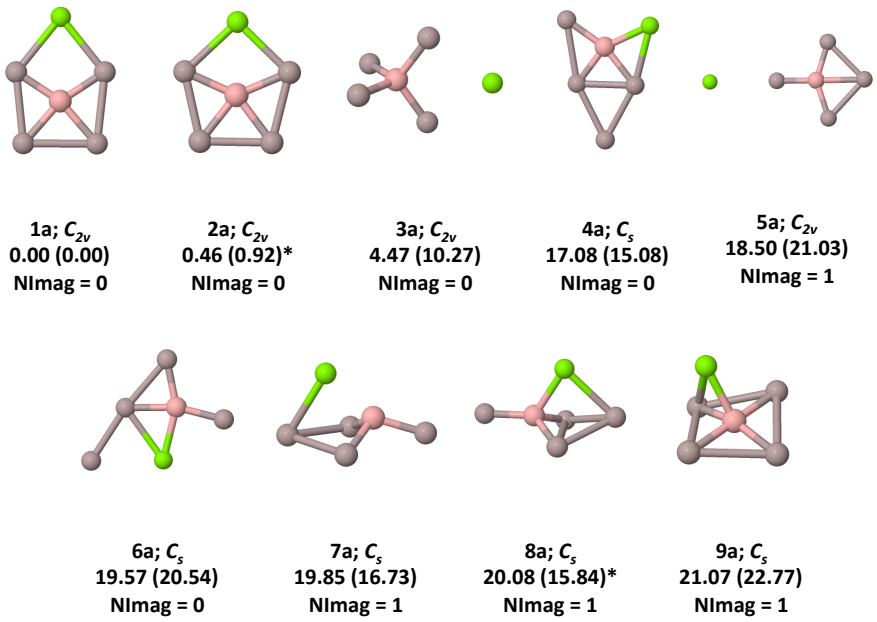

Figure 2. Low-lying singlet isomers of BAl_4Mg^-. ZPVE-corrected relative energies (in kcal mol^{-1}) are calculated at the ωB97XD/6-311++G(2d,2p) level. The same energies obtained at the CBS-QB3 level (at 0 K) are shown in parentheses. Values indicated with asterisk marks are calculated at the CCSD(T)/6-311++G(2d,2p)//ωB97XD/6-311++G(2d,2p) level. The number of imaginary frequencies (NImag) obtained for each stationary point are indicated underneath the geometries.

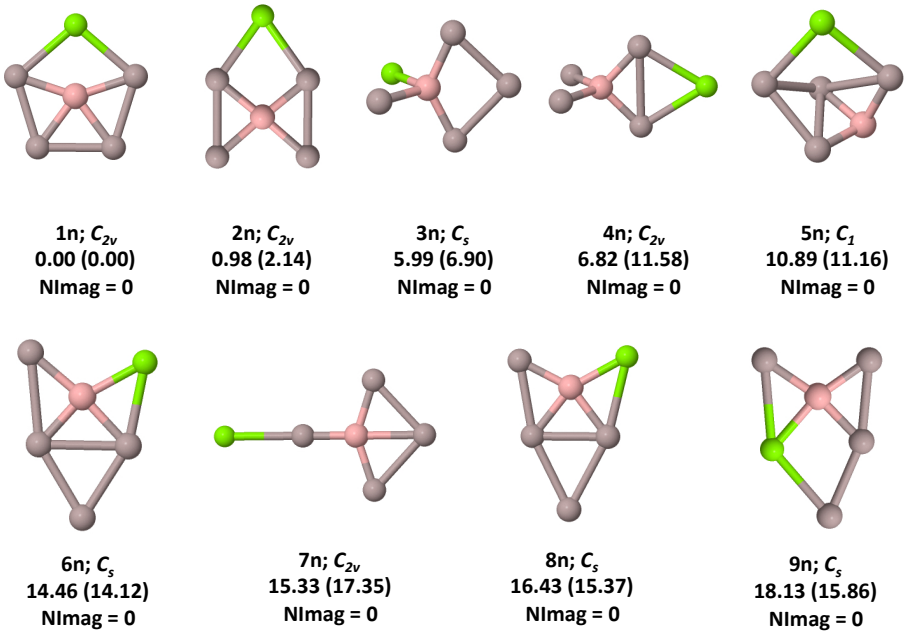

Figure 3. Low-lying doublet isomers of BAl_4Mg. ZPVE-corrected relative energies (in kcal mol^{-1}) are calculated at the UωB97XD/6-311++G(2d,2p) level. The same energies obtained at the CBS-QB3 level (at 0 K) are shown in parentheses.

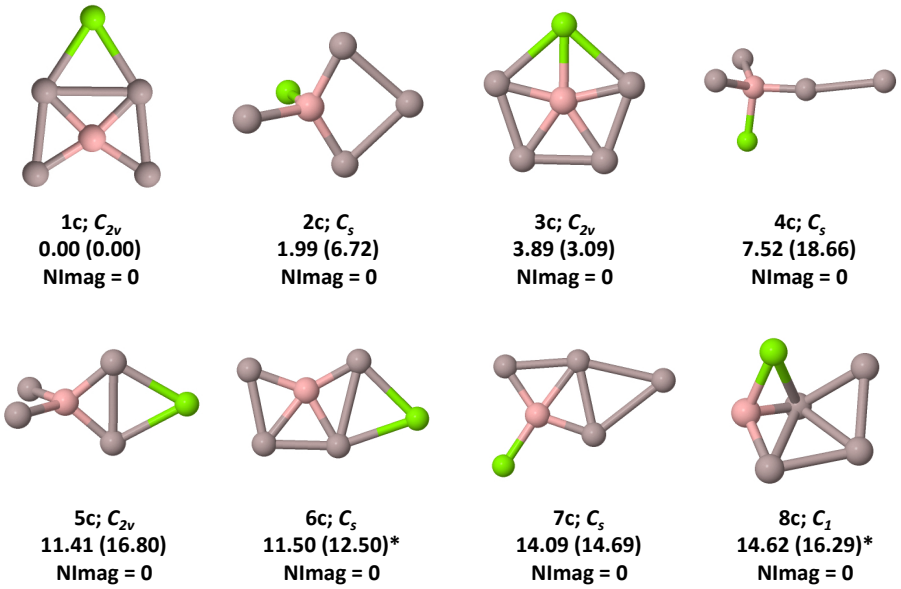

Figure 4. Low-lying singlet isomers of BAl_4Mg^+. ZPVE-corrected relative energies (in kcal mol^{-1}) are calculated at the ωB97XD/6-311++G(2d,2p) level. The same energies obtained at the CBS-QB3 level (at 0 K) are shown in parentheses. Values indicated with asterisk marks are calculated at the CCSD(T)/6-311++G(2d,2p)//ωB97XD/6-311++G(2d,2p) level.

3. Results and Discussion

3.1. Thermal Stability

Optimized geometries of the global minima (top row) and local minima (bottom row) of $BAl_4Mg^{-/0/+}$ containing either ptB or ppB atoms are shown in Figure 1. Bond lengths (in Å) and Wiberg bond indices (in green color) are shown for each isomer to justify the ptB or ppB scenario in Figure 1.

The low-lying isomers of $BAl_4Mg^{-/0/+}$ are shown in Figures 2–4, respectively. ZPVE-corrected relative energies obtained at the ωB97XD/6-311++G(2d,2p) (for anions and cations) and UωB97XD/6-311++G(2d,2p) (for neutrals) levels are given for each geometry. The same energies obtained at the CBS-QB3 level are given in parentheses. It is noted here that for a few isomers (**2a**, **8a**, **6c**, and **8c**), we could not calculate the relative energies using the composite method CBS-QB3. As the latter method carries out geometry optimization using the B3LYP functional [105–107] without any empirical dispersion corrections, in some cases, the geometry either transforms to a low-lying isomer or global minimum itself. Thus, the relative energy values are not given for geometries **2a**, **8a**, **6c**, and **8c** at the CBS-QB3 level. In these cases, the relative energy values given in parentheses were calculated at the CCSD(T)/6-311++G(2d,2p)//ωB97XD/6-311++G(2d,2p) level. In this work, we rely on the results obtained using the ωB97XD functional as it incorporates empirical dispersion corrections. For $BAl_4Mg^{-/+}$, singlet isomers with a ptB atom (**1a** and **1c**) were found to be the global minima. The second low-lying isomer for the anion (**2a**) lies only 0.48 kcal mol^{-1} above **1a** at the ωB97XD/6-311++G(2d,2p) level (see Figure 2). At CCSD(T)/6-311++G(2d,2p)//ωB97XD/6-311++G(2d,2p) level, this gap increases to 0.92 kcal mol^{-1}. For the cation, the second low-lying isomer (**2c**) contains a tetrahedral tetracoordinate boron atom, whereas the third isomer (**3c**) makes a clear case for the ppB atom (see Figure 4). Furthermore, **2c** and **3c** lie 1.99 and 3.89 kcal mol^{-1} above **1c** at the ωB97XD/6-311++G(2d,2p) level. At CBS-QB3 level, this trend is reversed and **3c** is more stable by 3.63 kcal mol^{-1} compared to **2c**. For BAl_4Mg neutral, the doublet isomer with ppB atom becomes the global minimum (**1n**; see Figure 3) and the second low-lying isomer (**2n**) that contains a ptB atom lies 0.98 kcal mol^{-1} above **1n** at the ωB97XD/6-311++G(2d,2p) level.

3.2. Kinetic Stability

To explore the kinetic stability of ptB and ppB isomers in $BAl_4Mg^{-/0/+}$, ab initio molecular dynamics simulations were carried out using the ADMP [96] approach as implemented in the Gaussian 16 program [102]. Six different isomers (see Figure 1) were considered for these simulations at a temperature of 298 K and 1 atm pressure for 2000 fs of time. The time evolution of the total energy (in a.u) plots for **1a** (anion; ptB) and **3c** (cation; ppB) are shown in Figures 5 and 6, respectively. For brevity, similar plots of four other isomers (**2a**, **1n**, **2n**, and **1c**) are shown in the supporting information. To show the alteration of the structure over the 2000 fs of time, we added snapshots at 400 fs intervals. These plots show balanced oscillations in energy and steadiness in geometries. This represents the kinetic stability of the minimum geometries. However, the trend of energy for the ppB of BAl_4Mg^+ (**3c**) is different from the others. The energy fluctuation is comparatively higher, and geometries (Figure 6) are not uniform. Here, at the end of the trajectory, it tends to form a 3D-like structure with lower energy. After seeing this trend, we also carried out additional simulations at 100 and 200 K for **3c** alone, which shows a balanced oscillation in energy and steadiness for this geometry. The time evolution of the total energy plot for **3c** at low temperatures is given in the supporting information for brevity. Overall, these results indirectly indicate that low-temperature measurements are necessary to trap the cation **3c** that exhibits a ppB atom.

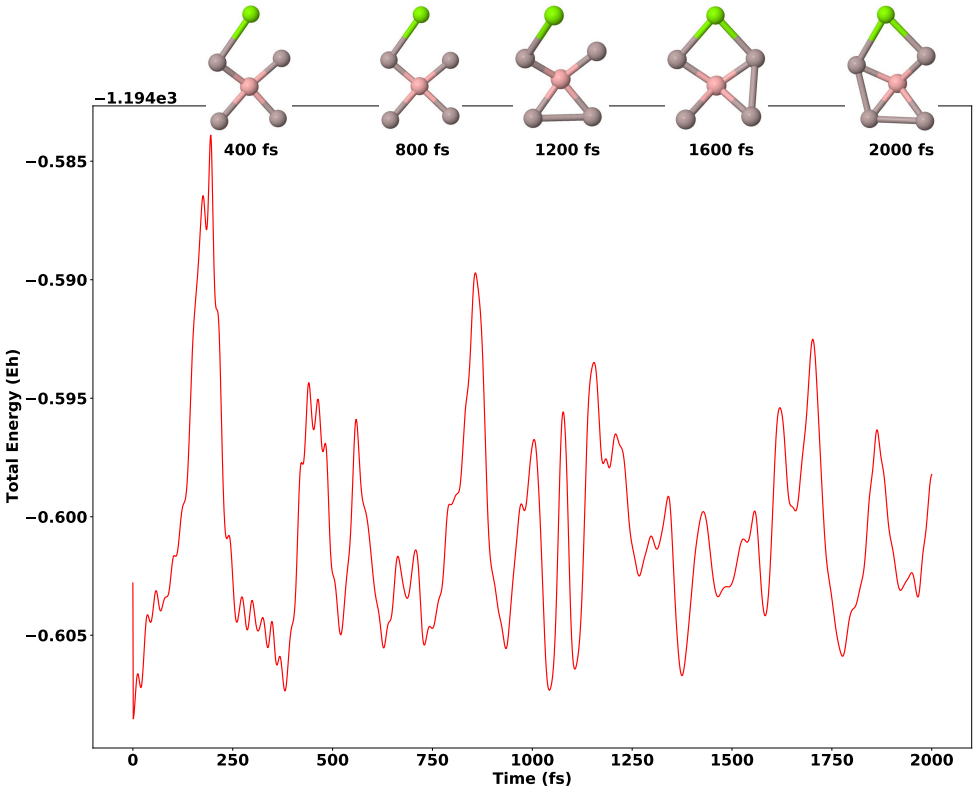

Figure 5. Energy evolution of ptB BAl_4Mg^- (**1a**) at 298 K for 2000 fs of time in the ADMP simulation performed at the ωB97XD/6-311++G(2d,2p) level.

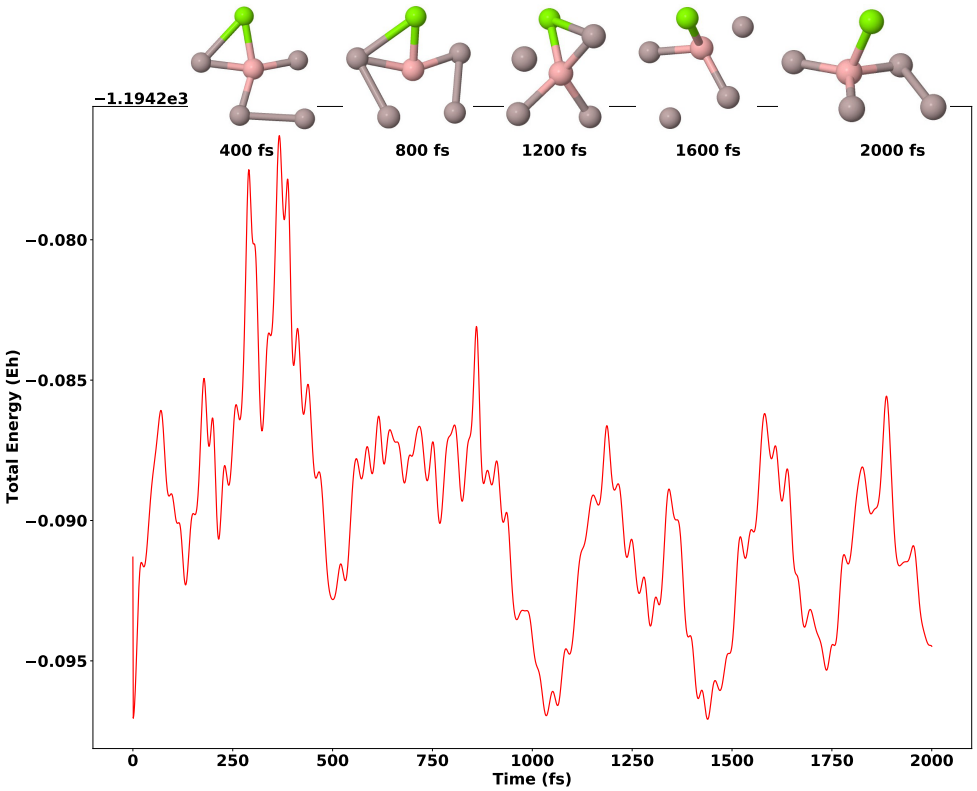

Figure 6. Energy evolution of ppB BAl_4Mg^+ (**3c**) at 298 K for 2000 fs of time in the ADMP simulation performed at the ωB97XD/6-311++G(2d,2p) level.

Furthermore, we analyzed the bond length of B1–Mg2 (Figure 7) for all the six geometries over the period of 2000 fs with the time interval of 250 fs. The bond length ranges from 3.063–3.657Å, 3.013–3.727Å, and 3.608–3.889Å for the ptB of BAl_4Mg^- (**1a**), BAl_4Mg (**2n**), and BAl_4Mg^+ (**1c**), respectively. Though the cationic ptB system in BAl_4Mg^+ contains 16 valence electrons, **1c** showed the maximum steadiness of energy as well as minimum change in bond length over the period of 2000 fs at 298 K compared to the other two ptB systems. The anionic ptB BAl_4Mg^- (**1a**; 18 *v. es*) shows a slightly lower scale of bond length variation (0.594Å) as compared to the neutral ptB BAl_4Mg (**2n**; 17*v. es*), which shows a variation of 0.714Å in bond lengths. Similarly, ppB BAl_4Mg^+ (**3c**) shows a maximum uniformity of the B1–Mg2 bond length (ranging from 2.139–2.315Å) compared to the other two ppB $BAl_4Mg^{-/0}$ systems (**2a** and **1n**). The bond length ranges for **2a** and **1n** are 2.523–3.366Å and 2.402–0.684Å, respectively. The latter two ppB systems cover the bond length variation from the ppB to the ptB region, and the fluctuations are quite high compared to the rest of the other four isomers. Furthermore, **2a** (18 *v. es*) depicts a lower range of bond length variation (0.843Å) compared to **1n** (17 *v. es*); i.e., 1.282Å.

In brief, the observation from the ADMP calculations suggests that all the geometries show steadiness in total energy (in a.u) over the period of 2000 fs. Maximum steadiness is perceived for ptB BAl_4Mg^+ (**1c**), whereas ppB BAl_4Mg^+ (**3c**) shows minimum steadiness in terms of total energy. Both the cationic form of ptB and ppB BAl_4Mg^+ demonstrate a smooth and minor change of the B1–Mg2 bond length. However, only the trajectory of ppB BAl_4Mg^+ produced a comparatively different geometry (3D like) from the planar tetracoordinate (2D) system. Nevertheless, simulations carried out at low temperatures (100 and 200 K) suggest that **3c** retains planarity.

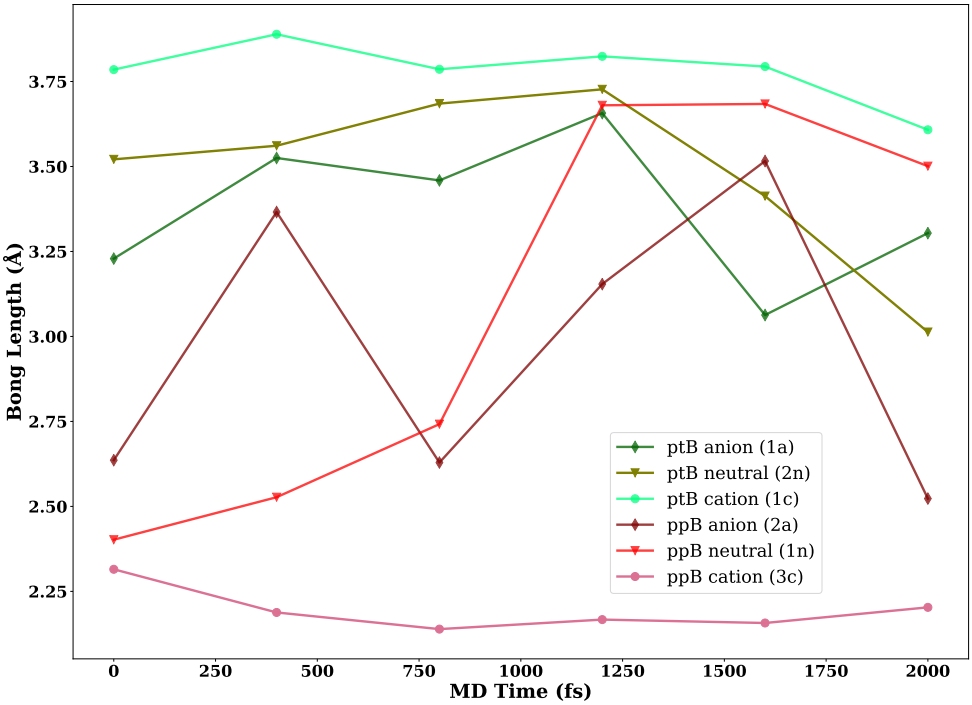

Figure 7. Bond length evolution of ptB and ppB $BAl_4Mg^{-/0/+}$ at 298 K for 2000 fs of time in the ADMP simulation performed at the (U)ωB97XD/6-311++G(2d,2p) level.

3.3. Natural Bond Orbital Analysis

We employed an NBO scheme for the distribution of natural charge over the $BAl_4Mg^{-/0/+}$ systems and analyzed WBI values for the boron atom coordination. The summary of the natural population analysis (NPA) charges for ptB (**1a**, **2n**, and **1c**) and ppB (**2a**, **1n**, and **3c**) systems are given in Table 1. This shows that a notable amount of charge transfer takes place from the peripheral aluminum atoms to the central boron atom. The natural charges on the central boron atom vary from -2.74 to -2.84 for ptB systems and -2.57 to -2.80 $|e|$ in ppB systems. The anions in both ptB and ppB show the highest negative charge on the boron atom. Moving from anion to neutral, the negative charge (absolute value) decreases in both the systems. As a result, an opposite trend is observed in the peripheral atoms; i.e., the positive charge increases. This also indicates that the charge transfer from the surrounding atoms to the boron atom decreases. The negative charges on the boron atom suggest that boron acts as a σ-acceptor in all the systems. From the valence electronic configuration of the boron given in Table 1, the $2p_x$ orbital population is significantly lower than that of the $2p_y$ and $2p_z$ orbital in the anion. The planner systems lie in the yz plane, and thus $2p_x$ orbital is perpendicular with respect to the molecular plane. The perpendicular boron $2p_x$ orbital participated in π-back bonding in the anionic system, whereas this is less probable in neutral and cationic species. The WBI_{total} is calculated for both ptB and ppB systems by taking the sum of four B–Al and one B–Mg values (see Table 2). The WBI values of B–Al (3,4) are in the range 0.89 to 0.94 in case of ptB and 0.77 to 0.84 in ppB systems which indicate covalent bonding with the central boron atom. However, B–Al (5,6) WBI values are somewhat smaller than B–Al (3,4), suggesting a lower covalency along that bond. The B–Mg WBI values are comparatively lower than those of the B–Al bonds. This implies a partial covalent character of this bond. The B–Mg WBI value increases from anion to cation in both ptB and ppB systems.

Table 1. The natural charges (q, |e|) of $BAl_4Mg^{-/0/+}$ containing ptB and ppB systems and their corresponding valence electronic configuration.

Type	Species	q_B	q_{Mg}	q_{Al3}	q_{Al4}	q_{Al5}	q_{Al6}	Valence Electronic Configuration of B
ptB	BAl_4Mg^- (**1a**)	−2.84	0.69	0.18	0.18	0.38	0.38	$2s^{1.37}\ 2p_x^{1.31}\ 2p_y^{1.52}\ 2p_z^{1.56}$
	BAl_4Mg (**2n**)	−2.79	0.90	0.25	0.25	0.69	0.69	$2s^{1.42}\ 2p_x^{1.37}\ 2p_y^{1.53}\ 2p_z^{1.39}$
	BAl_4Mg^+ (**1c**)	−2.74	1.13	0.33	0.33	0.97	0.97	$2s^{1.44}\ 2p_x^{1.35}\ 2p_y^{1.56}\ 2p_z^{1.32}$
ppB	BAl_4Mg^- (**2a**)	−2.80	0.83	0.16	0.16	0.32	0.32	$2s^{1.36}\ 2p_x^{1.26}\ 2p_y^{1.52}\ 2p_z^{1.60}$
	BAl_4Mg (**1n**)	−2.60	1.12	0.27	0.27	0.47	0.47	$2s^{1.40}\ 2p_x^{1.39}\ 2p_y^{1.52}\ 2p_z^{1.29}$
	BAl_4Mg^+ (**3c**)	−2.57	1.47	0.44	0.44	0.61	0.61	$2s^{1.43}\ 2p_x^{1.39}\ 2p_y^{1.56}\ 2p_z^{1.14}$

Table 2. Wiberg bond indices for $BAl_4Mg^{-/0/+}$ containing ptB and ppB systems.

Type	Species	B1-Mg2	B1-Al3	B1-Al4	B-Al5	B1-Al6	WBI_{total} on B
ptB	BAl_4Mg^- (**1a**)	0.074	0.907	0.907	0.651	0.651	3.190
	BAl_4Mg (**2n**)	0.064	0.889	0.889	0.614	0.614	3.064
	BAl_4Mg^+ (**1c**)	0.081	0.937	0.937	0.650	0.650	3.255
ppB	BAl_4Mg^- (**2a**)	0.045	0.842	0.842	0.726	0.726	3.180
	BAl_4Mg (**1n**)	0.119	0.769	0.769	0.683	0.683	3.023
	BAl_4Mg^+ (**3c**)	0.355	0.843	0.843	0.644	0.644	3.328

3.4. Molecular Orbital Analysis

Key molecular orbitals of $BAl_4Mg^{-/0/+}$ containing the ptB atom are given in Figure 8, whereas the same orbitals containing the ppB atom are given in Figure 9. Energies of the MOs obtained at the (U)ωB97XD/6-311++G(2d,2p) level are given in eV units. We further decomposed the MO composition with the natural atomic orbital method. For brevity, compositions and major contributions are given in the supporting information (see Table S7). The highest occupied molecular orbital (HOMO) for anionic and neutral ppB species is mainly composed of the B $2p_z$ orbital and Al (5,6) $3p_z$ orbital. All the p_z orbitals are in a bonding interaction. In contrast, the Mg 3*s* orbital contributes significantly in the case of anionic and neutral ppB BAl_4Mg. As the cationic species has one electron fewer than the neutral species, its HOMO resembles the HOMO–1 of the neutral and anionic species. It is composed of a B $2p_y$ orbital along with an Al (5,6) 3*s* orbital for ptB structure. For the ppB cationic case, besides the B $2p_z$ orbital, Al (3,4) 3*s* and $3p_z$ orbitals participate in HOMO. HOMO–3 of the anionic and neutral system and HOMO–1 of the cationic species are of π-type MO, which are formed from B $2p_x$ and Al $3p_x$ orbital. A significant contribution is made by the B $2p_x$ orbital. The HOMO–LUMO energy gaps (ΔE_{H-L}) are 4.59, 1.17, and 4.71 eV for anionic, neutral, and cationic ptB BAl_4Mg, respectively, and 0.43, 1.46, and 4.59 eV for anionic, neutral, and cationic ppB BAl_4Mg species, respectively. In the neutral BAl_4Mg, the HOMO has one unpaired electron; i.e., singly occupied MO (SOMO). Moving from anionic to cationic species, ΔE_{H-L} increases, indicating that cationic BAl_4Mg is more stable than its anionic form in both ptB and ppB cases. This is also evident from the lower HOMO energy compared to HOMO–1 of anionic and neutral BAl_4Mg. However, the Mg atomic orbital contribution is present only in HOMO–2 for all the ptB BAl_4Mg species. In the HOMO–2 of ptB BAl_4Mg^+, major contributions come from B $2p_z$, Mg 3*s*, and Al (3,4) $3p_y$, $3p_z$ orbitals. In contrast to anionic and neutral ptB BAl_4Mg, no significant contribution was found from boron. A similar type of composition is also found for the ppB BAl_4Mg HOMO–2 orbital. In the HOMO of both anionic and neutral ppB BAl_4Mg, there is a significant contribution from the Mg 3*s* orbital. So, there is a B–Mg coordination present for these species, which is absent in the ptB case. In the LUMO of cationic ppB BAl_4Mg, an orbital contribution from Mg 3*s* is found besides the B $2p_z$ orbital. This result suggests that, besides making bonds with four aluminum atoms, the central boron also has a fifth coordination with the Mg in the ppB species. As the neutral BAl_4Mg has one

unpaired electron, we also calculated the spin density (see Figure 10) for the ptB BAl_4Mg. The unpaired electron is delocalized on four Al atoms and with the boron $2p_z$ orbital. Al (3, 4) have the highest Mulliken spin density.

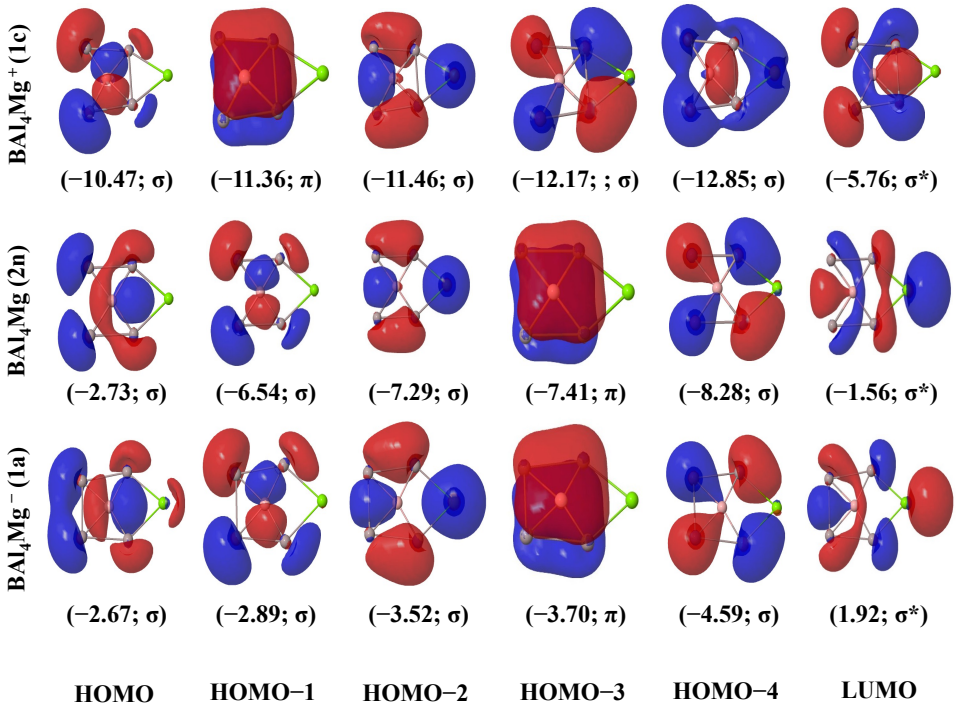

Figure 8. Molecular orbitals of $BAl_4Mg^{-/0/+}$ containing a ptB atom. Energies are in eV calculated at the (U)ωB97XD/6-311++G(2d,2p) level.

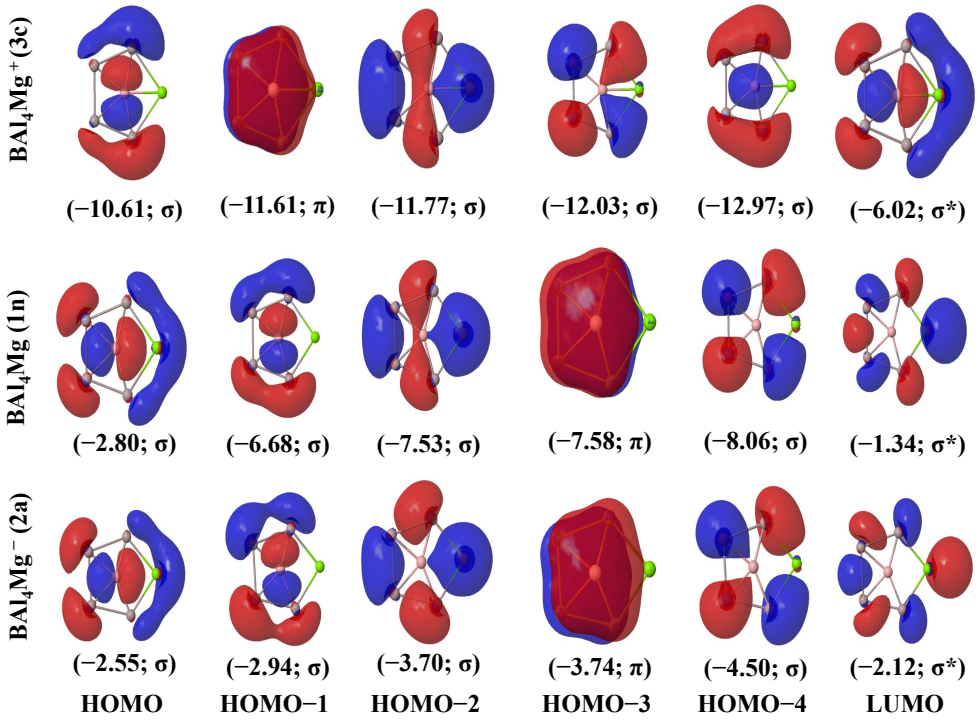

Figure 9. Molecular orbitals of $BAl_4Mg^{-/0/+}$ containing a ppB atom. Energies are in eV calculated at the (U)ωB97XD/6-311++G(2d,2p) level.

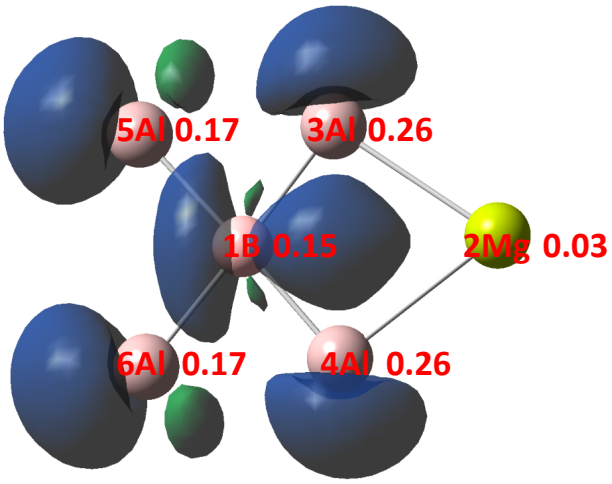

Figure 10. Spin density plot of BAl_4Mg (**2n**) containing a ptB atom calculated at the UωB97XD/6-311++G(2d,2p) level.

3.5. Adaptive Natural Density Partitioning (AdNDP) Analysis

We performed AdNDP analysis [97,98] as implemented in Multiwfn [104] for both ptB and ppB geometries of $BAl_4Mg^{-/0/+}$ to find the bonding scenarios in these systems. After NBO analysis, we mainly focused on the delocalized nc–2e bonds, where n starts from 3 to 6 (total number of atoms). All nc–2e bonding orbitals obtained for **1a**, **2n**, and **1c** that show the ptB atom are given in Figure 11. For the anion and cation, there are two 3c–2e and one 6c–2e σ bonds with an occupation number (ON) of 1.99 $|e|$ each and one 5c–2e π bond with an ON of 1.99 $|e|$. For neutral, the only difference that we observed was that the alpha orbital shows a maximum ON of 1.00 $|e|$ with a 6c–2e σ bond, whereas in beta, it is a 5c–2e σ bond. The 5c–2e π bond remains the same in both the cases. Overall, for all ptB cases, four multi-center two electron bonds (and thus eight electrons in total) that show the highest ONs support the idea of $2\pi/6\sigma$ double aromaticity. Likewise, for ppB geometries (**2a**, **1n**, and **3c**), we performed AdNDP analysis, and the nc–2e bonding orbitals are shown in Figure 12. For the anion, there are two 5c–2e σ bonds with an ON of 1.99 $|e|$ each, one 6c–2e σ bond with an ON of 2.00, and one 5c–2e π bond with an ON of 1.98 $|e|$. For the cation, one can clearly see that the delocalization is increased in the system as there are two 6c–2e σ bonds with an ON of 2.00 $|e|$ each, and one 5c–2e σ bond and one 5c–2e π bond both with an ON of 1.99 $|e|$ each. For neutral, we see similar trends in both alpha and beta cases. Once again, even for ppB systems, $2\pi/6\sigma$ double aromaticity is maintained.

3.6. NICS Analysis

In all these six isomers of $BAl_4Mg^{-/0/+}$, the π/σ-dual aromaticity can also be independently confirmed through NICS values. These values computed at 0 (on the ring) and 1 Å (above the ring) for ptB and ppB isomers at the (U)ωB97XD/6-311++G(2d,2p) level are shown in Figure 13. The pink dots represent the position of the ghost atoms. These positions are approximately chosen from the ring critical points obtained through AIM analysis. All the NICS values obtained are negative in all the cases. This indicates that both σ- (NICS(0)) and π-aromaticity (NICS(1)) are present in all these six different isomers, which supports the conclusion reached from the AdNDP bonding patterns.

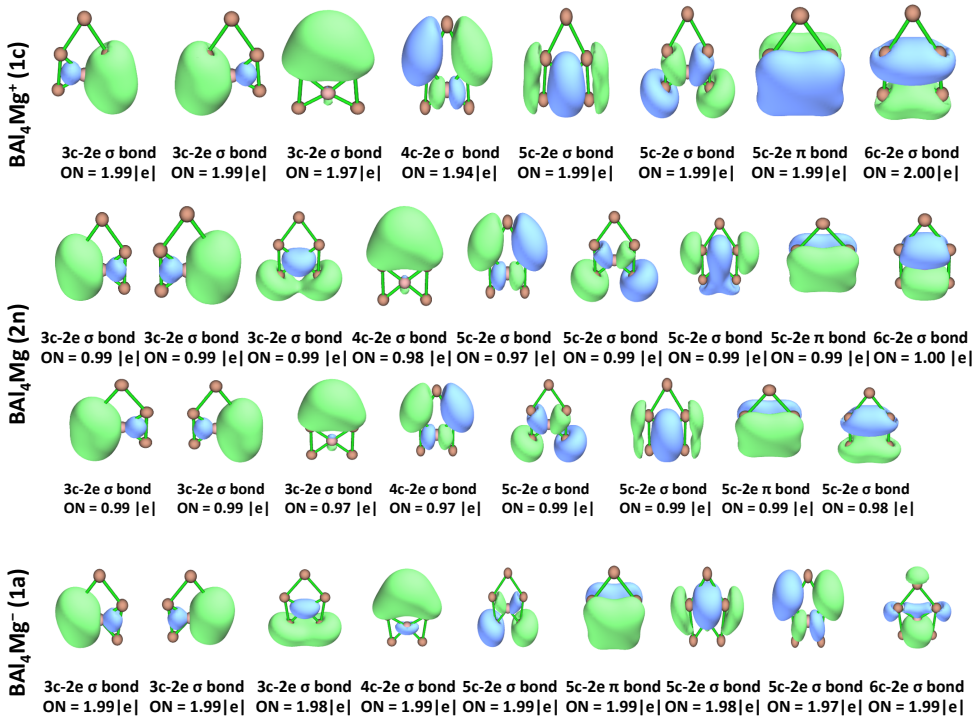

Figure 11. AdNDP bonding patterns of $BAl_4Mg^{-/0/+}$ containing ptB atom.

Figure 12. AdNDP bonding patterns of $BAl_4Mg^{-/0/+}$ containing ppB atom.

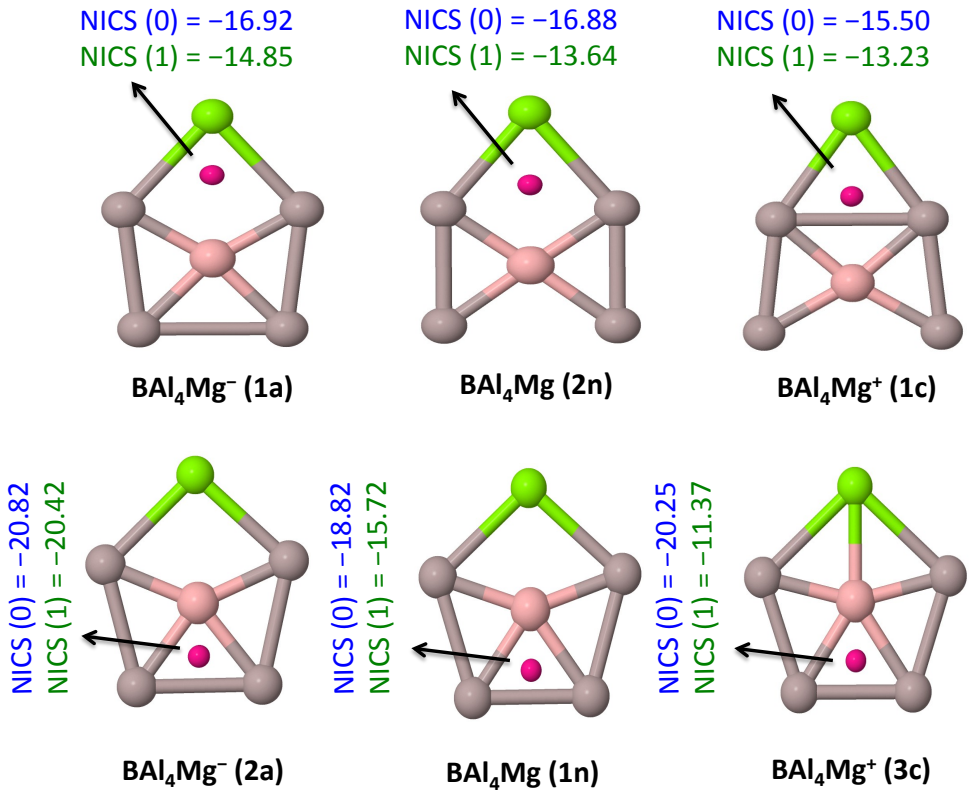

Figure 13. Nucleus-independent chemical shift (NICSs; in ppm) values for $BAl_4Mg^{-/0/+}$ calculated at the (U)ωB97XD/6-311++G(2d,2p) level. NICS (1) (green color) is calculated at 1 Å above the ring, whereas NICS (0) (blue color) refers to on the plane values.

3.7. AIM Analysis

We calculated various electron density descriptors at (3, –1) bond critical points for six different BAl_4Mg species. These results are summarized in Table 3. The contour diagram of $\nabla^2\rho(r)$ along with BCP paths and the corresponding ELF plots are shown in Figures 14 and 15. The existence of bonds between the central boron atom and four surrounding Al atoms is confirmed in both ptB (**1a**, **2n**, and **1c**) and ppB (**2a**, **1n**, and **3c**) systems. However, additional Mg atom coordination is found in the case of all the ppB species. Although the electron density at B–Mg BCP is lower compared to other BCPs, the low values of electron density ($\rho(r_c)$) at the BCPs indicate closed-shell type bonding. This is also evident from the positive $\nabla^2\rho(r_c)$, which indicates lower electron density at the BCPs. The total energy density $H(r_c) = G(r_c)+V(r_c)$ at the corresponding BCPs is negative for all the cases, suggesting a partial covalent character. The $G(r_c)/V(r_c)$ values are within 0.5 and 1, which indicate the absence of a non-covalent interaction and partial covalent character. This is also supported by the $G(r_c)/\rho(r_c)$ values, which are less than 1. The ELF plots show the extent of electron sharing among the central B to the peripheral atoms and electron density delocalization within the BAl_4Mg system. In the ppB system, there is electron delocalization between B and Mg besides B and Al, which is absent in the case of ptB BAl_4Mg species, which supports our previous analyses.

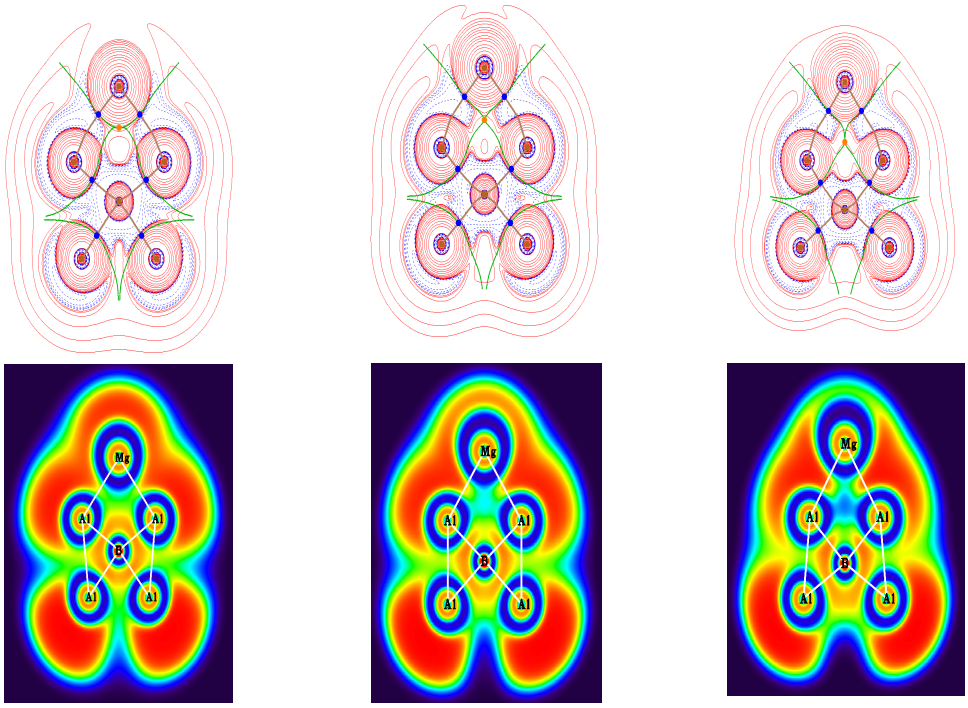

BAl_4Mg^- (1a) **BAl_4Mg (2n)** **BAl_4Mg^+ (1c)**

Figure 14. Contour map of the Laplacian of electron density ($\nabla^2\rho$(r)) with the bond paths (**top** row) and color-filled map of ELF (**bottom** row) for $BAl_4Mg^{-/0/+}$ containing the ptB atom calculated at the (U)ωB97XD/6-311++G(2d,2p) level.

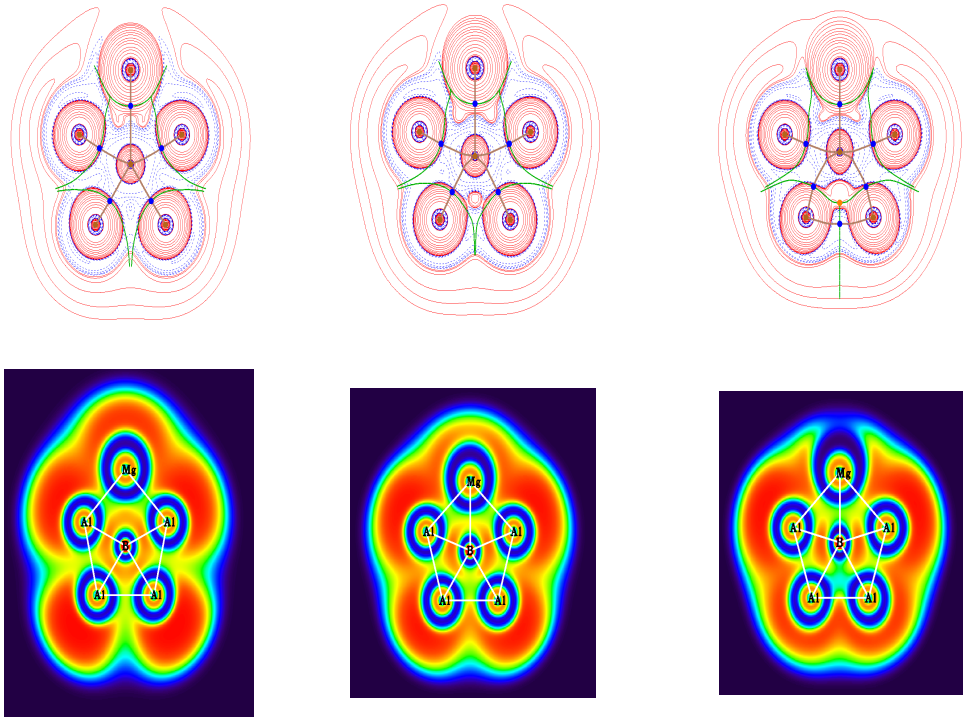

BAl_4Mg^- (2a) **BAl_4Mg (1n)** **BAl_4Mg^+ (3c)**

Figure 15. Contour map of the Laplacian of electron density ($\nabla^2\rho$(r)) with the bond paths (**top** row) and color-filled map of ELF for $BAl_4Mg^{-/0/+}$ containing ppB atom calculated at the (U)ωB97XD/6-311++G(2d,2p) level.

Table 3. Electron density descriptors (in a.u.) at the (3, –1) bond critical points (BCP) and ring critical point (RCP) obtained from the (U)ωB97XD/6-311++G(2d,2p) level for $BAl_4Mg^{-/0/+}$ (**1a**, **2n** and **1c**) with ptB atom. The topological parameters such as Lagrangian kinetic energy G(r_c), potential energy density V(r_c), energy density E(r_c) or H(r_c), $-G(r_c)/V(r_c)$, and $G(r_c)/\rho(r_c)$ at the critical points are also given.

System	BCP & RCP	$\rho(r_c)$	$\nabla^2\rho(r_c)$	$G(r_c)$	$V(r_c)$	$H(r_c)$	ELF	$-G(r_c)/V(r_c)$	$G(r_c)/\rho(r_c)$
1a	B1-Al5	0.0611	0.1090	0.0505	−0.0739	−0.0234	0.2250	0.6838	0.8266
	B1-Al4	0.0705	0.1370	0.0628	−0.0912	−0.0284	0.2320	0.6884	0.8909
	B1-Al6	0.0611	0.1090	0.0505	−0.0739	−0.0234	0.2250	0.6838	0.8266
	RCP	0.0213	0.0135	0.0075	−0.0115	−0.0041	0.2850	0.6460	0.3492
	Al3-Mg2	0.0243	0.0123	0.0088	−0.0144	−0.0057	0.3090	0.6065	0.3603
	B1-Al3	0.0705	0.1370	0.0628	−0.0912	−0.0284	0.2320	0.6884	0.8909
	Al4-Mg2	0.0243	0.0123	0.0088	−0.0144	−0.0057	0.3090	0.6065	0.3603
2n	B1-Al6	0.0611	0.1090	0.0505	−0.0738	−0.0233	0.2260	0.6839	0.8254
	B1-Al4	0.0688	0.1250	0.0590	−0.0867	−0.0277	0.2400	0.6805	0.8583
	B1-Al3	0.0688	0.1250	0.0590	−0.0867	−0.0277	0.2400	0.6805	0.8583
	B1-Al5	0.0611	0.1090	0.0505	−0.0738	−0.0233	0.2260	0.6839	0.8254
	RCP	0.0203	0.0104	0.0056	−0.0086	−0.0030	0.3840	0.6502	0.2762
	Al4-Mg2	0.0273	0.0068	0.0088	−0.0159	−0.0071	0.3960	0.5536	0.3215
	Al3-Mg2	0.0273	0.0068	0.0088	−0.0159	−0.0071	0.3960	0.5536	0.3215
1c	B1-Al4	0.0677	0.1040	0.0541	−0.0821	−0.0281	0.2630	0.6584	0.7985
	B1-Al3	0.0677	0.1040	0.0541	−0.0821	−0.0281	0.2630	0.6584	0.7985
	B1-Al6	0.0633	0.1090	0.0521	−0.0770	−0.0249	0.2350	0.6771	0.8231
	B1-Al5	0.0633	0.1090	0.0521	−0.0770	−0.0249	0.2350	0.6771	0.8231
	RCP	0.0197	0.0186	0.0069	−0.0092	−0.0023	0.2600	0.7533	0.3527
	Al4-Mg2	0.0289	0.0076	0.0095	−0.0172	−0.0077	0.4010	0.5550	0.3303
	Al3-Mg2	0.0289	0.0076	0.0095	−0.0172	−0.0077	0.4010	0.5550	0.3303
2a	B1-Al3	0.0689	0.1130	0.0570	−0.0857	−0.0287	0.2540	0.6651	0.8276
	B1-Al4	0.0689	0.1130	0.0570	−0.0857	−0.0287	0.2540	0.6651	0.8276
	B1-Al5	0.0625	0.1130	0.0526	−0.0769	−0.0243	0.2240	0.6841	0.8417
	B1-Al6	0.0625	0.1130	0.0526	−0.0769	−0.0243	0.2240	0.6841	0.8417
	B1-Mg2	0.0296	0.0557	0.0189	−0.0239	−0.0050	0.1550	0.7918	0.6395
1n	B1-Al4	0.0653	0.1100	0.0538	−0.0802	−0.0264	0.2430	0.6708	0.8231
	B1-Al3	0.0653	0.1100	0.0538	−0.0802	−0.0264	0.2430	0.6708	0.8231
	B1-Mg2	0.0336	0.0765	0.0248	−0.0305	−0.0057	0.1460	0.8137	0.7381
	B1-Al6	0.0585	0.0997	0.0472	−0.0695	−0.0223	0.2250	0.6791	0.8078
	B1-Al5	0.0585	0.0997	0.0472	−0.0695	−0.0223	0.2250	0.6791	0.8078
3c	B1-Al5	0.0541	0.0513	0.0343	−0.0558	−0.0215	0.2960	0.6149	0.6339
	B1-Al6	0.0541	0.0513	0.0343	−0.0558	−0.0215	0.2960	0.6149	0.6339
	B1-Mg2	0.0346	0.0739	0.0247	−0.0309	−0.0062	0.1540	0.7985	0.7135
	B1-Al4	0.0649	0.1240	0.0564	−0.0817	−0.0254	0.2220	0.6895	0.8681
	B1-Al3	0.0649	0.1240	0.0564	−0.0817	−0.0254	0.2220	0.6895	0.8681
	RCP	0.0378	0.0184	0.0137	−0.0229	−0.0091	0.4410	0.6006	0.3636
	Al6-Al5	0.0428	−0.0327	0.0061	−0.0204	−0.0143	0.8580	0.2999	0.1429

3.8. ALMO-EDA

We obtained an energy decomposition analysis (EDA) based on absolutely localized molecular orbitals (ALMO-EDA) calculations using the QCHEM program [103]. The total interaction energy is composed of four components as shown in Equation (1)

$$\begin{aligned} \Delta E_{int} &= E_{molecule} - \sum_{Z}^{frags} E_Z \\ &= \Delta E_{PREP} + \Delta E_{FRZ} + \Delta E_{POL} + \Delta E_{CT} \end{aligned} \quad (1)$$

Two fragments named X($BAl_4^{-/0/+}$) and Y(Mg) were considered to check the intramolecular interactions for all the six different structures (both ptB and ppB). The sharing

of interaction energy (ΔE_{int}) terms such as the preparation energy (ΔE_{PREP}), frozen energy (ΔE_{FRZ}), polarization energy (ΔE_{POL}), and charge transfer (ΔE_{CT}) are given in Figure 16. Herein, the ΔE_{FRZ} increases for ppB $BAl_4Mg^{-/0/+}$ compared to ptB $BAl_4Mg^{-/0/+}$. This term shows the energy change from the interaction of two fragments without the spin-coupling (SC), polarization (POL), or charge transfer (CT). It includes electrostatics, Pauli repulsion, exchange-correlation as well as dispersion corrections. The smaller value of ΔE_{PREP} shows that the geometry distortion and orbital rehybridization of each fragment to the original structure are very small in all cases. Two terms ΔE_{POL} and ΔE_{CT} demonstrate that polar, charge-shift, and ionic-type interactions are present in all the six cases. Similar observations for ptC systems are reported elsewhere [108]. Thus, our calculations for ptB/ppB systems support the notion that there is charge transfer from Y(Mg) to X($BAl_4^{-/0/+}$), as with ptC systems. Therefore, we can formulate our global and local minima of ptB and ppB as $[X]^-[Y]^+$.

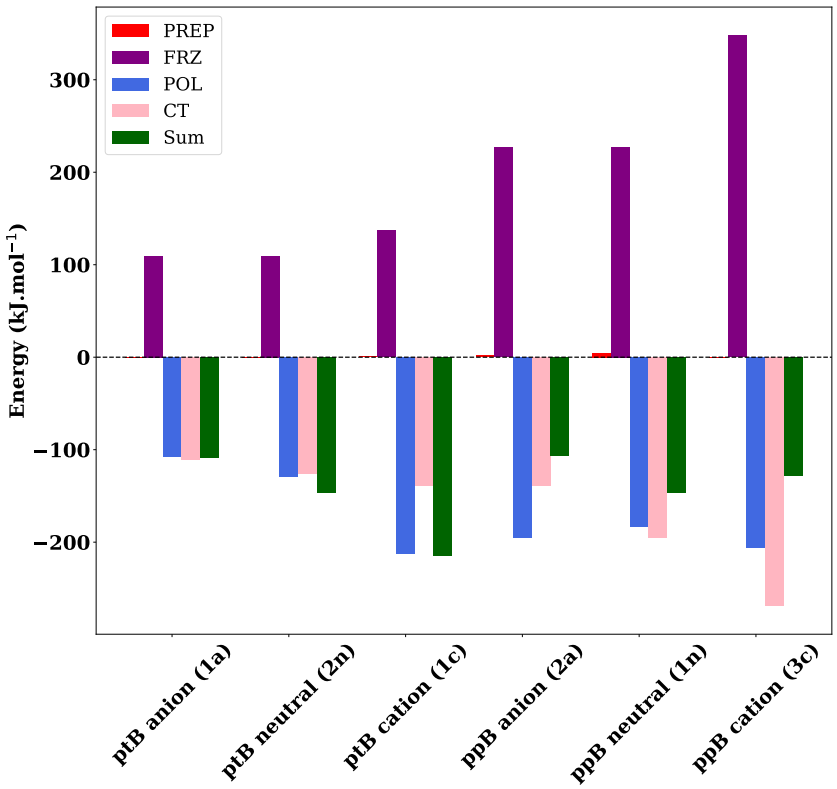

Figure 16. Total interaction energy containing four energy components for ptB and ppB systems of $BAl_4Mg^{-/0/+}$ obtained at the (U)ωB97XD/6-311++G(2d,2p) level.

4. Conclusions

Various isomers of $BAl_4Mg^{-/0/+}$ are theoretically identified for the first time using a tabu-search algorithm and chemical intuition. Three isomers (**1a**, **2n**, and **1c**) containing ptB atom and three isomers (**2a**, **1n**, **3c**) containing ppB atom are studied in detail. The global minima for the anion and cation contain a ptB atom with 18 and 16 valence electrons, respectively. The global minimum for the neutral exhibits a ppB atom with 17 valence electrons. The low-lying isomers of the anion (**2a**) and cation (**3c**) with 18 and 16 valence electrons, respectively, also exhibit a ppB atom. Ab initio MD simulations carried out at 298 K indicate that all isomers are kinetically stable except **3c**. At this temperature, the cation geometry (**3c**) breaks apart from its original structure. However, low-temperature simulations carried out at 100 and 200 K suggest that **3c** retains planarity and thus remains kinetically stable. Therefore, detecting **3c** through gas phase experiments is viable at low temperatures. The electron affinity value of BAl_4Mg is 2.15 eV, and therefore it is possible

to detect **1n** (ppB) through **1a** (ptB). Energy decomposition analysis carried out for all these six systems indicates that the interaction between fragments $BAl_4^{-/0/+}$ and Mg is ionic.

Supplementary Materials: The following are available online at https://www.mdpi.com/article/10.3390/atoms9040089/s1, Supplementary file 1: Supporting information for this paper.

Author Contributions: Conceptualization, V.S.T.; methodology, M.K., A.A. and V.S.T.; software, M.K., A.A., S.S.R.C. and V.S.T.; validation, V.S.T. and A.A.; formal analysis, M.K., S.R., S.G. and V.S.T.; investigation, M.K., S.R., S.G. and V.S.T.; resources, A.A. and V.S.T.; data curation, M.K., S.R., S.G., S.S.R.C. and V.S.T.; writing—original draft preparation, M.K., S.R., S.G. and V.S.T.; writing—review and editing, A.A. and V.S.T.; visualization, M.K., S.R., S.G., A.A. and V.S.T.; supervision, A.A. and V.S.T.; project administration, A.A. and V.S.T. All authors have read and agreed to the published version of the manuscript.

Funding: This research received no external funding. Computational support provided at the SDSU by DURIP Grant W911NF-10-1-0157 from the U.S. Department of Defense and by NSF CRIF Grant CHE-0947087 is gratefully acknowledged.

Institutional Review Board Statement: Not applicable.

Informed Consent Statement: Not applicable.

Data Availability Statement: Data available in article or Supplementary Materials.

Acknowledgments: We are thankful for the resources of the Supercomputing facility at the Indian Institute of Technology Kharagpur established under National Supercomputing Mission (NSM), Government of India and supported by the Center for Development of Advanced Computing (CDAC), Pune. MK thanks DST for the INSPIRE fellowship. VST thanks Andrew L. Cooksy (SDSU, San Diego) for providing additional computing time.

Conflicts of Interest: The authors declare no conflict of interest.

Abbreviations

The following abbreviations are used in this manuscript:

ADMP	Atom-Centered Density Matrix Propagation
AIMD	Ab Initio Molecular Dynamics
AdNDP	Adaptive Natural Density Partitioning
CMOs	Canonical Molecular Orbitals
DFT	Density Functional Theory
ELF	Electron Localization Function
MD	Molecular Dynamics
NBO	Natural Bond Order
NPA	Natural Population Analysis
NICS	Nucleus Independent Chemical Shift
ptB	Planar Tetracoordinate Boron
phC	Planar Hypercoordinate Carbon
ppB	Planar Pentacoordinate Boron
WBI	Wiberg Bond Index

References

1. Monkhorst, H.J. Activation Energy for Interconversion of Enantiomers Containing an Asymmetric Carbon Atom without Breaking Bonds. *Chem. Commun.* **1968**, 1111–1112. [CrossRef]
2. Hoffmann, R.; Alder, R.W.; Wilcox, C.F. Planar Tetracoordinate Carbon. *J. Am. Chem. Soc.* **1970**, *92*, 4992–4993. [CrossRef]
3. Würthwein, E.U.; von Ragué Schleyer, P. Planar Tetracoordinate Silicon. *Angew. Chem. Int. Ed. Engl.* **1979**, *18*, 553–554. [CrossRef]
4. Boldyrev, A.; Li, X.; Wang, L.S. Experimental Observation of Pentaatomic Tetracoordinate Planar Si- and Ge-Containing Molecules: MAl_4^- and MAl_4. *Angew. Chem. Int. Ed.* **2000**, *39*, 3307–3310. [CrossRef]
5. Ebner, F.; Greb, L. Calix[4]pyrrole Hydridosilicate: The Elusive Planar Tetracoordinate Silicon Imparts Striking Stability to Its Anionic Silicon Hydride. *J. Am. Chem. Soc.* **2018**, *140*, 17409–17412. [CrossRef]
6. Ghana, P.; Rump, J.; Schnakenburg, G.; Arz, M.I.; Filippou, A.C. Planar Tetracoordinated Silicon (ptSi): Room-Temperature Stable Compounds Containing Anti-van't Hoff/Le Bel Silicon. *J. Am. Chem. Soc.* **2020**, *143*, 420–432. [CrossRef] [PubMed]

7. Li, Y.; Li, F.; Zhou, Z.; Chen, Z. SiC_2 Silagraphene and Its One-Dimensional Derivatives: Where Planar Tetracoordinate Silicon Happens. *J. Am. Chem. Soc.* **2011**, *133*, 900–908. [CrossRef] [PubMed]
8. Yañez, O.; Vásquez-Espinal, A.; Pino-Rios, R.; Ferraro, F.; Pan, S.; Osorio, E.; Merino, G.; Tiznado, W. Exploiting electronic strategies to stabilize a planar tetracoordinate carbon in cyclic aromatic hydrocarbons. *Chem. Commun.* **2017**, *53*, 12112–12115.
9. Xu, J.; Ding, Y.H. Pentaatomic planar tetracoordinate silicon with 14 valence electrons: A large-scale global search of $SiX_nY_q^m$ (n + m = 4; q = 0, ±1, −2; X, Y = main group elements from H to Br). *J. Comput. Chem.* **2015**, *36*, 355–360. [CrossRef] [PubMed]
10. Thimmakondu, V.S.; Thirumoorthy, K. $Si_3C_2H_2$ Isomers with A Planar Tetracoordinate Carbon or Silicon Atom(s). *Comput. Theor. Chem.* **2019**, *1157*, 40–46. [CrossRef]
11. Von Ragué Schleyer, P.; Boldyrev, A.I. A New, General Strategy for Achieving Planar Tetracoordinate Geometries for Carbon and Other Second Row Periodic Elements. *J. Chem. Soc. Chem. Commun.* **1991**, 1536–1538. [CrossRef]
12. Menzel, M.; Steiner, D.; Winkler, H.J.; Schweikart, D.; Mehle, S.; Fau, S.; Frenking, G.; Massa, W.; Berndt, A. Compounds with Planar Tetracoordinate Boron Atoms: Anti van't Hoff/Le Bel Geometries without Metal Centers. *Angew. Chem. Int. Ed. Engl.* **1995**, *34*, 327–329. [CrossRef]
13. Berndt, A. Classical and Nonclassical Methyleneboranes. *Angew. Chem. Int. Ed. Engl.* **1993**, *32*, 985–1009. [CrossRef]
14. Sateesh, B.; Srinivas Reddy, A.; Narahari Sastry, G. Towards Design of the Smallest Planar Tetracoordinate Carbon and Boron Systems. *J. Comput. Chem.* **2007**, *28*, 335–343. [CrossRef]
15. Cui, Z.H.; Contreras, M.; Ding, Y.H.; Merino, G. Planar Tetracoordinate Carbon versus Planar Tetracoordinate Boron: The Case of CB_4 and Its Cation. *J. Am. Chem. Soc.* **2011**, *133*, 13228–13231. [CrossRef]
16. Feng, W.; Zhu, C.; Liu, X.; Zhang, M.; Geng, Y.; Zhao, L.; Su, Z. A BPt_4S_4 Cluster: A Planar Tetracoordinate Boron System with Three Charges All at Their Global Energy Minima. *New J. Chem.* **2020**, *44*, 767–772. [CrossRef]
17. Li, S.D.; Ren, G.M.; Miao, C.Q.; Jin, Z.H. M_4H_4X: Hydrometals (M = Cu, Ni) Containing Tetracoordinate Planar Nonmetals (X = B, C, N, O). *Angew. Chem. Int. Ed.* **2004**, *43*, 1371–1373. [CrossRef]
18. Ebner, F.; Wadepohl, H.; Greb, L. Calix[4]pyrrole Aluminate: A Planar Tetracoordinate Aluminum(III) Anion and Its Unusual Lewis Acidity. *J. Am. Chem. Soc.* **2019**, *141*, 18009–18012. [CrossRef]
19. Ebner, F.; Mainik, P.; Greb, L. Calix[4]pyrrolato Aluminates: The Effect of Ligand Modification on the Reactivity of Square-Planar Aluminum Anions. *Chem. Eur. J.* **2021**, *27*, 5120–5124. [CrossRef]
20. Cui, Z.H.; Ding, Y.H. $NXAl_3^+$ (X = N, P, As): Penta-atomic Planar Tetracoordinate Nitrogen with N-X multiple bonding. *Phys. Chem. Chem. Phys.* **2011**, *13*, 5960–5966. [CrossRef]
21. Jimenez-Izal, E.; Saeys, M.; Alexandrova, A.N. Metallic and Magnetic 2D Materials Containing Planar Tetracoordinated C and N. *J. Phys. Chem. C* **2016**, *120*, 21685–21690. [CrossRef]
22. Li, S.D.; Ren, G.M.; Miao, C.Q. (M4H3X)2B2O2: Hydrometal Complexes (M = Ni, Mg) Containing Double Tetracoordinate Planar Nonmetal Centers (X = C, N). *J. Phys. Chem. A* **2005**, *109*, 259–261. [CrossRef] [PubMed]
23. Driess, M.; Aust, J.; Merz, K.; van Wüllen, C. van't Hoff-Le Bel Stranger: Formation of a Phosphonium Cation with a Planar Tetracoordinate Phosphorus Atom. *Angew. Chem. Int. Ed.* **1999**, *38*, 3677–3680. [CrossRef]
24. Wang, H.; Liu, F.L. Theoretical Study on Neutral Molecules with Square Planar Tetracoordinate Oxygen O(B)4 Arrangements. *ACS Omega* **2020**, *5*, 24513–24519. [CrossRef]
25. Castillo-Toraya, G.; Orozco-Ic, M.; Dzib, E.; Zarate, X.; Ortíz-Chi, F.; Cui, Z.H.; Barroso, J.; Merino, G. Planar Tetracoordinate Fluorine Atoms. *Chem. Sci.* **2021**, *12*, 6699–6704. [CrossRef] [PubMed]
26. Erker, G. Planar-Tetracoordinate Carbon: Making Stable Anti-van't Hoff/Le Bel Compounds. *Comment. Inorg. Chem.* **1992**, *13*, 111–131. [CrossRef]
27. Röttger, D.; Erker, G. Compounds Containing Planar-Tetracoordinate Carbon. *Angew. Chem. Int. Ed. Engl.* **1997**, *36*, 812–827. [CrossRef]
28. Cotton, F.A.; Millar, M. The Probable Existence of A Triple Bond Between Two Vanadium Atoms. *J. Am. Chem. Soc.* **1977**, *99*, 7886. [CrossRef]
29. Boldyrev, A.I.; Simons, J. Tetracoordinated Planar Carbon in Pentaatomic Molecules. *J. Am. Chem. Soc.* **1998**, *120*, 7967–7972. [CrossRef]
30. Li, X.; Wang, L.S.; Boldyrev, A.I.; Simons, J. Tetracoordinated Planar Carbon in the Al_4C^- Anion. A Combined Photoelectron Spectroscopy and ab Initio Study. *J. Am. Chem. Soc.* **1999**, *121*, 6033–6038. [CrossRef]
31. Keese, R. Carbon Flatland: Planar Tetracoordinate Carbon and Fenestranes. *Chem. Rev.* **2006**, *106*, 4787–4808. [CrossRef] [PubMed]
32. Xu, J.; Zhang, X.; Yu, S.; Ding, Y.H.; Bowen, K.H. Identifying the Hydrogenated Planar Tetracoordinate Carbon: A Combined Experimental and Theoretical Study of CAl_4H and CAl_4H^-. *J. Phys. Chem. Lett.* **2017**, *8*, 2263–2267. [CrossRef] [PubMed]
33. Li, X.; Zhang, H.F.; Wang, L.S.; Geske, G.; Boldyrev, A. Pentaatomic Tetracoordinate Planar Carbon, $[CAl_4]^{2-}$: A New Structural Unit and Its Salt Complexes. *Angew. Chem. Int. Ed.* **2000**, *39*, 3630–3632. [CrossRef]
34. Collins, J.B.; Dill, J.D.; Jemmis, E.D.; Apeloig, Y.; von Ragué Schleyer, P.; Seeger, R.; Pople, J.A. Stabilization of Planar Tetracoordinate Carbon. *J. Am. Chem. Soc.* **1976**, *98*, 5419–5427. [CrossRef]
35. Merino, G.; Méndez-Rojas, M.A.; Beltrán, H.I.; Corminboeuf, C.; Heine, T.; Vela, A. Theoretical Analysis of the Smallest Carbon Cluster Containing a Planar Tetracoordinate Carbon. *J. Am. Chem. Soc.* **2004**, *126*, 16160–16169. [CrossRef]

36. Suresh, C.H.; Frenking, G. Direct 1-3 Metal-Carbon Bonding and Planar Tetracoordinated Carbon in Group 6 Metallacyclobutadienes. *Organometallics* **2010**, *29*, 4766–4769. [CrossRef]
37. Thirumoorthy, K.; Karton, A.; Thimmakondu, V.S. From High-Energy C_7H_2 Isomers with A Planar Tetracoordinate Carbon Atom to An Experimentally Known Carbene. *J. Phys. Chem. A* **2018**, *122*, 9054–9064. [CrossRef] [PubMed]
38. Raghunathan, S.; Yadav, K.; Rojisha, V.C.; Jaganade, T.; Prathyusha, V.; Bikkina, S.; Lourderaj, U.; Priyakumar, U.D. Transition Between [R]- and [S]-Stereoisomers without Bond Breaking. *Phys. Chem. Chem. Phys.* **2020**, *22*, 14983–14991. [CrossRef] [PubMed]
39. Yang, L.M.; Ganz, E.; Chen, Z.; Wang, Z.X.; von Ragué Schleyer, P. Four Decades of the Chemistry of Planar Hypercoordinate Compounds. *Angew. Chem. Int. Ed.* **2015**, *54*, 9468–9501. [CrossRef]
40. Zheng, H.F.; Yu, S.; Hu, T.D.; Xu, J.; Ding, Y.H. CAl_3X (X = B/Al/Ga/In/Tl) with 16 Valence Electrons: Can Planar Tetracoordinate Carbon Be Stable? *Phys. Chem. Chem. Phys.* **2018**, *20*, 26266–26272. [CrossRef]
41. Yañez, O.; Vásquez-Espinal, A.; Báez-Grez, R.; Rabanal-León, W.A.; Osorio, E.; Ruiz, L.; Tiznado, W. Carbon Rings Decorated with Group 14 Elements: New Aromatic Clusters Containing Planar Tetracoordinate Carbon. *New J. Chem.* **2019**, *43*, 6781–6785.
42. Thirumoorthy, K.; Thimmakondu, V.S. Flat Crown Ethers with Planar Tetracoordinate Carbon Atoms. *Int. J. Quantum Chem.* **2021**, *121*, e26479. [CrossRef]
43. Yadav, K.; Lourderaj, U.; Priyakumar, U.D. Stereomutation in Tetracoordinate Centers via Stabilization of Planar Tetracoordinated Systems. *Atoms* **2021**, *9*, 79. [CrossRef]
44. Van't Hoff, J.H. A Suggestion Looking to the Extension Into Space of the Structural Formulas at Present Used in Chemistry. And A Note Upon the Relation Between the Optical Activity and the Chemical Constitution of Organic Compounds. *Arch. Neerl. Sci. Exactes Nat.* **1874**, *9*, 445–454.
45. Le-Bel, J.A. On the Relations Which Exist Between the Atomic Formulas of Organic Compounds and the Rotatory Power of Their Solutions. *Bull. Soc. Chim. Fr.* **1874**, *22*, 337–347.
46. Cui, Z.H.; Ding, Y.H.; Cabellos, J.L.; Osorio, E.; Islas, R.; Restrepo, A.; Merino, G. Planar tetracoordinate carbons with a double bond in CAl_3E clusters. *Phys. Chem. Chem. Phys.* **2015**, *17*, 8769–8775. [CrossRef] [PubMed]
47. Nandula, A.; Trinh, Q.T.; Saeys, M.; Alexandrova, A.N. Origin of Extraordinary Stability of Square-Planar Carbon Atoms in Surface Carbides of Cobalt and Nickel. *Angew. Chem. Int. Ed.* **2015**, *54*, 5312–5316. [CrossRef] [PubMed]
48. Guo, J.C.; Feng, L.Y.; Dong, C.; Zhai, H.J. Ternary 12-electron $CBe_3X_3^+$ (X = H, Li, Na, Cu, Ag) Clusters: Planar Tetracoordinate Carbons and Superalkali Cations. *Phys. Chem. Chem. Phys.* **2019**, *21*, 22048–22056. [CrossRef] [PubMed]
49. Thirumoorthy, K.; Cooksy, A.; Thimmakondu, V.S. $Si_2C_5H_2$ Isomers – Search Algorithms Versus Chemical Intuition. *Phys. Chem. Chem. Phys.* **2020**, *22*, 5865–5872. [CrossRef] [PubMed]
50. Jimenez-Halla, J.O.C.; Wu, Y.B.; Wang, Z.X.; Islas, R.; Heine, T.; Merino, G. CAl_4Be and $CAl_3Be_2^-$: Global Minima with A Planar Pentacoordinate Carbon Atom. *Chem. Commun.* **2010**, *46*, 8776–8778. [CrossRef] [PubMed]
51. Crigger, C.; Wittmaack, B.K.; Tawfik, M.; Merino, G.; Donald, K.J. Plane and Simple: Planar Tetracoordinate Carbon Centers in Small Molecules. *Phys. Chem. Chem. Phys.* **2012**, *14*, 14775. [CrossRef] [PubMed]
52. Priyakumar, U.D.; Sastry, G.N. A system with three contiguous planar tetracoordinate carbons is viable: A computational study on a $C_6H_6^{2+}$ isomer. *Tetrahedron Lett.* **2004**, *45*, 1515–1517. [CrossRef]
53. Vogt-Geisse, S.; Wu, J.I.C.; von Ragué Schleyer, P.; Schaefer, H.F. Bonding, aromaticity, and planar tetracoordinated carbon in Si_2CH_2 and Ge_2CH_2. *J. Mol. Model* **2015**, *21*, 217. [CrossRef]
54. Job, N.; Karton, A.; Thirumoorthy, K.; Cooksy, A.L.; Thimmakondu, V.S. Theoretical Studies of SiC_4H_2 Isomers Delineate Three Low-Lying Silylidenes Are Missing in the Laboratory. *J. Phys. Chem. A* **2020**, *124*, 987–1002. [CrossRef] [PubMed]
55. Thirumoorthy, K.; Chandrasekaran, V.; Cooksy, A.L.; Thimmakondu, V.S. Kinetic Stability of $Si_2C_5H_2$ Isomer with a Planar Tetracoordinate Carbon Atom. *Chemistry* **2021**, *3*, 13–27. [CrossRef]
56. Job, N.; Khatun, M.; Thirumoorthy, K.; CH, S.S.R.; Chandrasekaran, V.; Anoop, A.; Thimmakondu, V.S. $CAl_4Mg^{0/-}$: Global Minima with a Planar Tetracoordinate Carbon Atom. *Atoms* **2021**, *9*, 24. [CrossRef]
57. Saumya, M.J.; Raghi, K.R.; Sherin, D.R.; Haridas, K.R.; Manojkumar, T.K. Butterfly Methanes: Designing a Novel Class of anti-van't Hoff Carbons. *ChemPhysChem* **2020**, *21*, 2272–2278. [CrossRef]
58. Das, P.; Chattaraj, P.K. In Silico Studies on Selected Neutral Molecules, CGa_2Ge_2, $CAlGaGe_2$, and $CSiGa_2Ge$ Containing Planar Tetracoordinate Carbon. *Atoms* **2021**, *9*, 65. [CrossRef]
59. Becker, S.; Dietze, H.J. Cluster Ions in the Laser Mass Spectra of Boron Carbide. *Int. J. Mass Spectrom.* **1988**, *82*, 287–298. [CrossRef]
60. Pei, Y.; An, W.; Ito, K.; von Ragué Schleyer, P.; Zeng, X.C. Planar Pentacoordinate Carbon in CAl_5^+: A Global Minimum. *J. Am. Chem. Soc.* **2008**, *130*, 10394–10400. [CrossRef]
61. Guo, J.C.; Feng, L.Y.; Zhang, X.Y.; Zhai, H.J. Star-Like $CBe_5Au_5^+$ Cluster: Planar Pentacoordinate Carbon, Superalkali Cation, and Multifold (π and σ) Aromaticity. *J. Phys. Chem. A* **2018**, *122*, 1138–1145. [CrossRef]
62. Castro, A.C.; Martínez-Guajardo, G.; Johnson, T.; Ugalde, J.M.; Wu, Y.B.; Mercero, J.M.; Heine, T.; Donald, K.J.; Merino, G. CBe_5E-(E = Al, Ga, In, Tl): Planar Pentacoordinate Carbon in Heptaatomic Clusters. *Phys. Chem. Chem. Phys.* **2012**, *14*, 14764–14768. [CrossRef] [PubMed]
63. Ravell, E.; Jalife, S.; Barroso, J.; Orozco-Ic, M.; Hernandez-Juarez, G.; Ortiz-Chi, F.; Pan, S.; Cabellos, J.L.; Merino, G. Structure and Bonding in CE_5^- (E = Al-Tl) Clusters: Planar Tetracoordinate Carbon vs Pentacoordinate Carbon. *Chem.-Asian J.* **2018**, *13*, 1467–1473. [CrossRef] [PubMed]

64. Pan, S.; Cabellos, J.L.; Orozco-Ic, M.; Chattaraj, P.K.; Zhao, L.; Merino, G. Planar Pentacoordinate Carbon in CGa_5^+ Derivatives. *Phys. Chem. Chem. Phys.* **2018**, *20*, 12350–12355. [CrossRef] [PubMed]
65. Vassilev-Galindo, V.; Pan, S.; Donald, J.K.; Merino, G. Planar Pentacoordinate Carbons. *Nat. Chem. Rev.* **2018**, *2*, 0114. [CrossRef]
66. Thimmakondu, V.S. Hypervalent Carbon Atoms in a Ferrocene Dication Derivative-$[Fe(Si_2C_5H_2)_2]^{2+}$. *ChemRxiv* **2021**. [CrossRef]
67. Exner, K.; von Ragué Schleyer, P. Planar Hexacoordinate Carbon: A Viable Possibility. *Science* **2000**, *290*, 1937–1940. [CrossRef]
68. Averkiev, B.B.; Zubarev, D.Y.; Wang, L.M.; Huang, W.; Wang, L.S.; Boldyrev, A.I. Carbon Avoids Hypercoordination in CB_6^-, CB_6^{2-}, and $C_2B_5^-$ Planar Carbon-Boron Clusters. *J. Am. Chem. Soc.* **2008**, *130*, 9248–9250. [CrossRef] [PubMed]
69. Ito, K.; Chen, Z.; Corminboeuf, C.; Wannere, C.S.; Zhang, X.H.; Li, Q.S.; von Ragué Schleyer, P. Myriad Planar Hexacoordinate Carbon Molecules Inviting Synthesis. *J. Am. Chem. Soc.* **2007**, *129*, 1510–1511. [CrossRef] [PubMed]
70. Wu, Y.B.; Duan, Y.; Lu, G.; Lu, H.G.; Yang, P.; von Ragué Schleyer, P.; Merino, G.; Islas, R.; Wang, Z.X. D_{3h} $CN_3Be_3^+$ and $CO_3Li_3^+$: Viable Planar Hexacoordinate Carbon Prototypes. *Phys. Chem. Chem. Phys.* **2012**, *14*, 14760–14763. [CrossRef] [PubMed]
71. Zhang, C.F.; Han, S.J.; Wu, Y.B.; Lu, H.G.; Lu, G. Thermodynamic Stability versus Kinetic Stability: Is the Planar Hexacoordinate Carbon Species D_{3h} $CN_3Mg_3^+$ Viable? *J. Phys. Chem. A* **2014**, *118*, 3319–3325. [CrossRef]
72. Zhai, H.J.; Alexandrova, A.N.; Birch, K.A.; Boldyrev, A.I.; Wang, L.S. Hepta- and Octacoordinate Boron in Molecular Wheels of Eight- and Nine-Atom Boron Clusters: Observation and Confirmation. *Angew. Chem. Int. Ed.* **2003**, *42*, 6004–6008. [CrossRef]
73. Kalita, A.J.; Rohman, S.S.; Kashyap, C.; Ullah, S.S.; Guha, A.K. Double aromaticity in a $BBe_6H_6^+$ cluster with a planar hexacoordinate boron structure. *Chem. Commun.* **2020**, *56*, 12597–12599. [CrossRef] [PubMed]
74. Averkiev, B.B.; Wang, L.M.; Huang, W.; Wang, L.S.; Boldyrev, A.I. Experimental and Theoretical Investigations of CB8-: Towards Rational Design of Hypercoordinated Planar Chemical Species. *Phys. Chem. Chem. Phys.* **2009**, *11*, 9840. [CrossRef] [PubMed]
75. Sarkar, R.; Baishya, D.; Mahapatra, S. Photodetachment Spectroscopy of Carbon Doped Anionic Boron Cluster, CB9-: A Theoretical Study. *Chem. Phys.* **2018**, *515*, 679–691. [CrossRef]
76. Kalita, A.J.; Rohman, S.S.; Kashyap, C.; Ullah, S.S.; Baruah, I.; Guha, A.K. Planar Pentacoordinate Nitrogen in a Pseudo-Double-Aromatic $NBe_5H_4^+$ Cluster. *Inorg. Chem.* **2020**, *59*, 17880–17883. [CrossRef] [PubMed]
77. Wang, Y.; Li, F.; Li, Y.; Chen, Z. Semi-Metallic Be_5C_2 Monolayer Global Minimum with Quasi-Planar Pentacoordinate Carbons and Negative Poisson's Ratio. *Nat. Commun.* **2016**, *7*, 11488. [CrossRef]
78. Li, Y.; Liao, Y.; Chen, Z. Be_2C Monolayer with Quasi-Planar Hexacoordinate Carbons: A Global Minimum Structure. *Angew. Chem. Int. Ed.* **2014**, *53*, 7248–7252. [CrossRef]
79. Minyaev, R.M.; Gribanova, T.N.; Minkin, V.I.; Starikov, A.G.; Hoffmann, R. Planar and Pyramidal Tetracoordinate Carbon in Organoboron Compounds. *J. Org. Chem.* **2005**, *70*, 6693. [CrossRef]
80. Zhang, C.; Wang, P.; Liang, J.; Jia, W.; Cao, Z. Theoretical study on a family of organic molecules with planar tetracoordinate carbon. *J. Mol. Struct. THEOCHEM* **2010**, *941*, 41–46. [CrossRef]
81. Islas, R.; Heine, T.; Ito, K.; von Ragué Schleyer, P.; Merino, G. Boron Rings Enclosing Planar Hypercoordinate Group 14 Elements. *J. Am. Chem. Soc.* **2007**, *129*, 14767. [CrossRef]
82. Erhardt, S.; Frenking, G.; Chen, Z.; von Ragué Schleyer, P. Aromatic Boron Wheels with More than One Carbon Atom in the Center: C_2B_8, $C_3B_9^{3+}$, and $C_5B_{11}^+$. *Angew. Chem. Int. Ed.* **2005**, *44*, 1078–1082. [CrossRef] [PubMed]
83. Nandi, S.; McAnanama-Brereton, S.R.; Waller, M.P.; Anoop, A. A Tabu-Search Based Strategy for Modeling Molecular Aggregates and Binary Reactions. *Comput. Theor. Chem.* **2017**, *1111*, 69–81. [CrossRef]
84. Khatun, M.; Majumdar, R.S.; Anoop, A. A Global Optimizer for Nanoclusters. *Front. Chem.* **2019**, *7*, 644. [CrossRef] [PubMed]
85. Neese, F. Software Update: The ORCA Program System, Version 4.0. *Wiley Interdiscip. Rev. Comput. Mol. Sci.* **2018**, *8*, e1327. [CrossRef]
86. Perdew, J.P.; Burke, K.; Wang, Y. Generalized Gradient Approximation for the Exchange-Correlation Hole of a Many-Electron System. *Phys. Rev. B* **1996**, *54*, 16533. [CrossRef]
87. Weigend, F.; Ahlrichs, R. Balanced Basis Sets of Split Valence, Triple Zeta Valence and Quadruple Zeta Valence Quality for H to Rn: Design and Assessment of Accuracy. *Phys. Chem. Chem. Phys.* **2005**, *7*, 3297–3305. [CrossRef]
88. Grimme, S.; Antony, J.; Ehrlich, S.; Krieg, H. A Consistent and Accurate Ab Initio Parametrization of Density Functional Dispersion Correction (DFT-D) for the 94 Elements H-Pu. *J. Chem. Phys.* **2010**, *132*, 154104. [CrossRef]
89. Becke, A.D.; Johnson, E.R. Exchange-Hole Dipole Moment and the Dispersion Interaction. *J. Chem. Phys.* **2005**, *122*, 154104. [CrossRef]
90. Grimme, S.; Ehrlich, S.; Goerigk, L. Effect of the Damping Function in Dispersion Corrected Density Functional Theory. *J. Comput. Chem.* **2011**, *32*, 1456–1465. [CrossRef]
91. Chai, J.D.; Head-Gordon, M. Long-Range Corrected Hybrid Density Functionals with Damped Atom–Atom Dispersion Corrections. *Phys. Chem. Chem. Phys.* **2008**, *10*, 6615–6620. [CrossRef]
92. Krishnan, R.; Binkley, J.S.; Seeger, R.; Pople, J.A. Self-Consistent Molecular Orbital Methods. XX. A Basis Set for Correlated Wave Functions. *J. Chem. Phys.* **1980**, *72*, 650–654. [CrossRef]
93. Clark, T.; Chandrasekhar, J.; Spitznagel, G.W.; von Ragué Schleyer, P. Efficient Diffuse Function-Augmented Basis Sets for Anion Calculations. III. The 3-21+G Basis Set for First-Row Elements, Li-F. *J. Comput. Chem.* **1983**, *4*, 294–301. [CrossRef]
94. Montgomery, J.A.; Frisch, M.J.; Ochterski, J.W.; Petersson, G.A. A Complete Basis Set Model Chemistry. VI. Use of Density Functional Geometries and Frequencies. *J. Chem. Phys.* **1999**, *110*, 2822–2827. [CrossRef]

95. Bauernschmitt, R.; Ahlrichs, R. Stability Analysis for Solutions of the Closed Shell Kohn–Sham Equation. *J. Chem. Phys.* **1996**, *104*, 9047–9052. [CrossRef]
96. Schlegel, H.B.; Millam, J.M.; Iyengar, S.S.; Voth, G.A.; Daniels, A.D.; Scuseria, G.E.; Frisch, M.J. Ab Initio Molecular Dynamics: Propagating the Density Matrix with Gaussian Orbitals. *J. Chem. Phys.* **2001**, *114*, 9758–9763. [CrossRef]
97. Zubarev, D.Y.; Boldyrev, A.I. Developing Paradigms of Chemical Bonding: Adaptive Natural Density Partitioning. *Phys. Chem. Chem. Phys.* **2008**, *10*, 5207–5217. [CrossRef] [PubMed]
98. Zubarev, D.Y.; Boldyrev, A.I. Revealing Intuitively Assessable Chemical Bonding Patterns in Organic Aromatic Molecules via Adaptive Natural Density Partitioning. *J. Org. Chem.* **2008**, *73*, 9251–9258. [CrossRef]
99. Reed, A.E.; Weinstock, R.B.; Weinhold, F. Natural Population Analysis. *J. Chem. Phys.* **1985**, *83*, 735–746. [CrossRef]
100. Glendening, E.D.; Weinhold, F. Natural Resonance Theory: I. General Formalism. *J. Comput. Chem.* **1998**, *19*, 593–609. [CrossRef]
101. Von Ragué Schleyer, P.; Maerker, C.; Dransfeld, A.; Jiao, H.; van Eikema Hommes, N.J.R. Nucleus-Independent Chemical Shifts: A Simple and Efficient Aromaticity Probe. *J. Am. Chem. Soc.* **1996**, *118*, 6317–6318. [CrossRef]
102. Frisch, M.J.; Trucks, G.W.; Schlegel, H.B.; Scuseria, G.E.; Robb, M.A.; Cheeseman, J.R.; Scalmani, G.; Barone, V.; Petersson, G.A.; Nakatsuji, H.; et al. *Gaussian 16 Revision B.01*; Gaussian Inc.: Wallingford, CT, USA, 2016.
103. Shao, Y.; Gan, Z.; Epifanovsky, E.; Gilbert, A.T.; Wormit, M.; Kussmann, J.; Lange, A.W.; Behn, A.; Deng, J.; Feng, X.; et al. Advances in molecular quantum chemistry contained in the Q-Chem 4 program package. *Mol. Phys.* **2015**, *113*, 184–215. [CrossRef]
104. Lu, T.; Chen, F. Multiwfn: A Multifunctional Wavefunction Analyzer. *J. Comput. Chem.* **2012**, *33*, 580–592. [CrossRef] [PubMed]
105. Lee, C.; Yang, W.; Parr, R.G. Development of the Colle-Salvetti correlation-energy formula into a functional of the electron density. *Phys. Rev. B* **1988**, *37*, 785–789. [CrossRef] [PubMed]
106. Becke, A.D. Density-functional exchange-energy approximation with correct asymptotic behavior. *Phys. Rev. A* **1988**, *38*, 3098–3100. [CrossRef]
107. Becke, A.D. Density-Functional Thermochemistry. III. The Role of Exact Exchange. *J. Chem. Phys.* **1993**, *98*, 5648–5652. [CrossRef]
108. Zheng, H.F.; Xu, J.; Ding, Y.H. A Sixteen-Valence-Electron Carbon-Group 13 Family with Global Penta-Atomic Planar Tetracoordinate Carbon: An Ionic Strategy. *Phys. Chem. Chem. Phys.* **2020**, *22*, 3975–3982. [CrossRef] [PubMed]